JGP Journal of General Physiology

ARTICLE

Different arrhythmia-associated calmodulin mutations have distinct effects on cardiac SK channel regulation

Hannah A. Ledford[1], Seojin Park[2], Duncan Muir[1], Ryan L. Woltz[1], Lu Ren[1], Phuong T. Nguyen[3], Padmini Sirish[1], Wenying Wang[2], Choong-Ryoul Sihn[2], Alfred L. George Jr.[4], Björn C. Knollmann[5], Ebenezer N. Yamoah[2], Vladimir Yarov-Yarovoy[3], Xiao-Dong Zhang[1,6], and Nipavan Chiamvimonvat[1,6]

Calmodulin (CaM) plays a critical role in intracellular signaling and regulation of Ca^{2+}-dependent proteins and ion channels. Mutations in CaM cause life-threatening cardiac arrhythmias. Among the known CaM targets, small-conductance Ca^{2+}-activated K^+ (SK) channels are unique, since they are gated solely by beat-to-beat changes in intracellular Ca^{2+}. However, the molecular mechanisms of how CaM mutations may affect the function of SK channels remain incompletely understood. To address the structural and functional effects of these mutations, we introduced prototypical human CaM mutations in human induced pluripotent stem cell–derived cardiomyocyte-like cells (hiPSC-CMs). Using structural modeling and molecular dynamics simulation, we demonstrate that human calmodulinopathy-associated CaM mutations disrupt cardiac SK channel function via distinct mechanisms. CaM_{D96V} and CaM_{D130G} mutants reduce SK currents through a dominant-negative fashion. By contrast, specific mutations replacing phenylalanine with leucine result in conformational changes that affect helix packing in the C-lobe, which disengage the interactions between apo-CaM and the CaM-binding domain of SK channels. Distinct mutant CaMs may result in a significant reduction in the activation of the SK channels, leading to a decrease in the key Ca^{2+}-dependent repolarization currents these channels mediate. The findings in this study may be generalizable to other interactions of mutant CaMs with Ca^{2+}-dependent proteins within cardiac myocytes.

Introduction

Calmodulin (CaM) is a multifunctional Ca^{2+}-binding protein that orchestrates a wide range of intracellular signaling and critical cellular processes (Crivici and Ikura, 1995; Chin and Means, 2000). CaM, a 17-kD protein, is encoded by three distinct genes in humans, namely *CALM1*, *CALM2*, and *CALM3*, each of which encodes an identical CaM protein. CaM is composed of N- and C-terminal lobes linked by a flexible helix (Babu et al., 1985; Heidorn and Trewhella, 1988). Each lobe contains two EF hands, canonical Ca^{2+}-binding motifs, with the N-lobe having slightly lower Ca^{2+}-binding affinity (Watterson et al., 1980; Klevit et al., 1984; Thulin et al., 1984). Ca^{2+} binding to the EF hands results in structural and functional changes in target molecules (Saimi and Kung, 2002).

Recent studies have provided genetic links between human heritable CaM mutations and several types of cardiac arrhythmia syndromes leading to sudden cardiac death, including long QT syndrome (LQTS; Crotti et al., 2013; Reed et al., 2015; Boczek et al., 2016), catecholaminergic polymorphic ventricular tachycardia (CPVT; Nyegaard et al., 2012), and familial idiopathic ventricular fibrillation (IVF; Hwang et al., 2014). N54I and N98S mutations in CaM are associated with cases of CPVT with altered CaM-ryanodine receptor 2 (RYR2) function; F90L has been shown to be linked to IVF; and D96V, D130G, and F142L are associated with LQTS.

LQTS mutations of CaM have been shown to reside at or near Ca^{2+} coordinating sites within the EF hands of the C-lobe of CaM (Limpitikul et al., 2014; Jensen et al., 2018). *CALM1*-D130G and *CALM2*-D96V mutations alter highly conserved aspartic acid residues that bind Ca^{2+} ions in EF-hand domains IV and III, respectively. The *CALM1*-F142L mutation results in an alteration of the energetic coupling of Ca^{2+} binding and the conformational change associated with CaM activation (Crotti et al., 2013). All three LQTS-associated mutations show reduced Ca^{2+} affinity in the C-lobe by 5-, 13-, and 53-fold for F142L, D96V, and D130G,

[1]Division of Cardiovascular Medicine, Department of Internal Medicine, School of Medicine, University of California, Davis, Davis, CA; [2]Department of Physiology and Cell Biology, University of Nevada, Reno, Reno, NV; [3]Department of Physiology and Membrane Biology, School of Medicine, University of California, Davis, Davis, CA; [4]Department of Pharmacology, Northwestern University Feinberg School of Medicine, Chicago, IL; [5]Vanderbilt Center for Arrhythmia Research and Therapeutics, Department of Medicine, School of Medicine, Vanderbilt University, Nashville, TN; [6]Department of Veterans Affairs, Northern California Health Care System, Mather, CA.

Correspondence to Nipavan Chiamvimonvat: nchiamvimonvat@ucdavis.edu; Xiao-Dong Zhang: xdzhang@ucdavis.edu.

© 2020 Ledford et al. This article is distributed under the terms of an Attribution–Noncommercial–Share Alike–No Mirror Sites license for the first six months after the publication date (see http://www.rupress.org/terms/). After six months it is available under a Creative Commons License (Attribution–Noncommercial–Share Alike 4.0 International license, as described at https://creativecommons.org/licenses/by-nc-sa/4.0/).

Downloaded from http://rupress.org/jgp/article-pdf/152/12/e202012667/1800962/jgp_202012667.pdf by guest on 07 February 2026

respectively (Crotti et al., 2013). These mutations in CaM result in a significant reduction in Ca^{2+}-dependent inactivation (CDI) of $Ca_v1.2$ L-type Ca^{2+} channel (LTCC; Peterson et al., 1999; Zühlke et al., 1999; Zühlke et al., 2000). In contrast, CPVT mutations in CaM impart little-to-mild reduction of Ca^{2+}-binding affinity (Nyegaard et al., 2012).

Clearly, CaM exerts its function on a number of targets in cardiomyocytes, including RYR2 (Meissner, 1986; Fukuda et al., 2014; Hwang et al., 2014; Nomikos et al., 2014; Vassilakopoulou et al., 2015), $K_v7.1$ (or KCNQ1; Shamgar et al., 2006; Sachyani et al., 2014; Sun and MacKinnon, 2017), LTCCs ($Ca_v1.2$, $Ca_v1.3$; Liang et al., 2003; Halling et al., 2006; Findeisen and Minor, 2010), and small-conductance Ca^{2+}-activated K^+ (SK) channels (Xia et al., 1998; Schumacher et al., 2001). Among the CaM-targets, SK channels are unique because the channels are voltage independent and are gated solely by beat-to-beat changes in intracellular Ca^{2+} (Ca^{2+}_i). SK channels harbor a highly conserved CaM-binding domain (CaMBD); the gating of the channels is controlled by Ca^{2+} binding and unbinding to CaM associated with SK channels (Xia et al., 1998). Thus, CaM serves as the high affinity Ca^{2+} sensor for SK channels. Studies on human calmodulinopathy have provided evidence for the critical roles of CaM in the functional regulation of SK channels (Yu et al., 2016; Saljic et al., 2019). However, the mechanistic effects on SK channels by mutations in CaM remain incompletely understood.

Ca^{2+}-activated K^+ (K_{Ca}) channels can be divided into three main subfamilies based on their electrophysiological, pharmacological, and molecular phenotypes. These include large-conductance Ca^{2+}- and voltage-activated K^+ channels (BK), the intermediate-conductance K_{Ca} channels (IK or SK4), and the small-conductance K_{Ca} channels (SK1, 2, and 3; Köhler et al., 1996; Ishii et al., 1997; Joiner et al., 1997; Vergara et al., 1998). SK4 channels have intermediate single-channel conductance and are sensitive to charybdotoxin. In contrast, SK channels have small single-channel conductance and are sensitive to apamin. Recent cryo-EM structure of the SK4 channel–CaM complex (Lee and MacKinnon, 2018) reveals atomic details of the SK channel C-terminal interaction with the C-lobe of CaM, demonstrating that the C-lobe binds to the channel constitutively, while the N-lobe interacts with the S4-S5 linker in a Ca^{2+}-dependent manner. The S4-S5 linker undergoes conformational changes upon CaM binding to open the channel pore (Lee and MacKinnon, 2018). CaM opens SK channels with a median effective intracellular concentration of Ca^{2+} of ∼100–400 nM (Köhler et al., 1996; Xia et al., 1998).

Here, we take advantage of the SK4 channel–CaM complex structure as a template for Rosetta molecular modeling, combined with MD simulation and biochemical and functional analyses to test the effects of the known CaM mutations on cardiac SK2 channel functions. Specifically, we tested the hypothesis that human CaM mutations linked to sudden cardiac death disrupt SK channel function by distinct mechanisms. Mutations in the Ca^{2+}-binding domain of CaM (*CALM1*-D130G, *CALM2*-D96V) result in a dominant-negative (DN) effect, while specific mutations with phenylalanine to leucine (*CALM1*-F90L and -F142L) disrupt the interactions between apo-CaM with the CaMBD of SK channels. SK currents have been shown to be prominently expressed not only in atrial myocytes (Xu et al., 2003; Zhang et al., 2015) but also in cardiac Purkinje cells (Reher et al., 2017). Indeed, Purkinje cells have been shown to be the probable site of origin of cardiac arrhythmias, including in patients with heritable arrhythmia syndromes (Haïssaguerre et al., 2002; Wilde et al., 2019). Additionally, SK channels have been shown to be expressed and play important roles in pacemaking cells, including sinoatrial and atrioventricular nodes (Zhang et al., 2008; Torrente et al., 2017). Distinct mutant CaMs may result in a significant reduction in the activation of the SK channels, leading to a decrease in the key Ca^{2+}-dependent repolarization currents mediated by SK channels, exacerbating the effects of CaM mutations in LQTS or IVF.

Materials and methods

Plasmid construction

Human filamin A (FLNA) in pREP4 vector (Life Technologies) was a kind gift from Dr. Paramita M. Ghosh (University of California Davis, Davis, CA). α-Actinin2 cDNA in pcDNA3 vector was a kind gift from Dr. David Fedida (University of British Columbia, Vancouver, BC, Canada; Cukovic et al., 2001). Construction of SK2 expression plasmids for heterologous expression in human embryonic kidney (HEK) 293 cells was as follows: full-length human cardiac SK2 cDNA was subcloned into pIRES2-EGFP (Takara Bio USA, Inc.) to obtain pSK2-IRES-EGFP plasmid. SK2 channel fusion constructs were generated harboring WT CaM (CaM_{WT}; human SK2 [hSK2]-G_4-CaM_{WT}) or mutant CaMs (hSK2-G_4 mutant CaM) to specifically occupy the CaMBD of SK2 channels with CaM_{WT} or mutant CaMs using flexible linkers (glycine linkers) as previously described by Mori et al. (2004).

To study the subcellular localization of the SK2 channel subunit, modified human influenza hemagglutinin (HA) tag was inserted into the extracellular S1-S2 loop of the channel. Specifically, modified HA epitope was flanked with the ClC-5 chloride channel D1-D2 loop to increase accessibility and inserted in the end of the S1-S2 loop of the SK2 channel subunit as we described previously (Kim et al., 2011). The inserted amino acid sequence was NSEH**YPYDVPDYA**VTFEERDKCPEWNC. The epitope is shown in bold. Epitope tags were generated by recombination polymerase chain reaction and verified by automated sequencing.

HEK 293 cells and plasmid transfection

HEK 293 cells were maintained in Dulbecco's modified Eagle's medium supplemented with 10% FBS. Cell lines were maintained at 37°C in a humidified atmosphere containing 5% CO_2. All cell culture reagents were purchased from Life Technologies. HEK 293 cells were transfected using the following plasmid compositions: pSK2-IRES-EGFP, in combination with pREP4-FLNA and pcDNA3–α-actinin2, with WT (CaM_{WT}) or mutant CaM (1 µg for each plasmid), using Lipofectamine 2000 (Life Technologies) according to the manufacturer's protocol. The 1:1 ratio of the plasmids was determined to be most optimal for SK2 current expression in our prior published studies (Rafizadeh et al., 2014).

Downloaded from http://rupress.org/jgp/article-pdf/152/12/e202012667/1800962/jgp_202012667.pdf by guest on 07 February 2026

Patch-clamp recordings

Whole-cell Ca^{2+}-activated K^+ current ($I_{K,Ca}$) was recorded from transfected HEK 293 cells and human induced pluripotent stem cell (hiPSC)–derived cardiomyocyte-like cells (hiPSC-CMs) at room temperature using conventional patch-clamp techniques as previously described (Xu et al., 2003). For current recordings, the extracellular solution contained (in mM) 140 *N*-methylglucamine, 4 KCl, 1 $MgCl_2$, 5 glucose, and 10 HEPES, pH 7.4, with HCl. The internal solution contained (in mM) 144 potassium gluconate, 1.15 $MgCl_2$, 5 EGTA, 10 HEPES, and $CaCl_2$ yielding a free cytosol Ca^{2+} concentration of 500 nM, using the Maxchelator software by C. Patton of Stanford University as we have previously described (Zhang et al., 2017). The pH was adjusted to 7.25 using KOH. To isolate apamin-sensitive SK currents, extracellular solution containing apamin (10 or 100 nM) was applied during the recordings, and the difference currents between the control and the apamin-containing solution were calculated to be the apamin-sensitive currents. The current was elicited from a holding potential of −55 mV using a voltage ramp protocol ranging from −120 to +60 mV with a 2-s duration.

For hiPSC-CM recordings, 0.006 mM CaM_{WT} or mutant CaM peptides was added to the intracellular solution, and the recordings were performed 3 min after forming whole-cell recording for complete dialysis of the peptides.

All recordings were performed using 3 M KCl agar bridges. Cell capacitance was calculated as the ratio of total charge (the integrated area under the current transient) to the magnitude of the pulse (20 mV). Currents were normalized to cell capacitance to obtain the current density. Series resistance was compensated electronically. In all experiments, a series resistance compensation of ≥90% was obtained. The currents were recorded using Axopatch 200A amplifier (Molecular Devices), filtered at 1 kHz using a four-pole Bessel filter, and digitized at a sampling frequency of 5 kHz. Data acquisition and analysis were performed using pClamp 10 software (Molecular Devices) and Origin Software (OriginLab).

Immunofluorescence confocal laser scanning microscopy of HEK 293 cells

HEK 293 cells were cotransfected with human cardiac SK2-HA (SK2 channel with the extracellular HA tag) together with α-actinin, FLNA, and CaM_{WT} or mutant CaM, using Lipofectamine (Life Technologies; catalog #11668-019) as we previously described (Rafizadeh et al., 2014). After blocking with 1% BSA (Sigma; catalog #A7030) under nonpermeabilization (NP) condition, SK2 channels localized on the cell membrane were labeled with monoclonal anti-HA antibody (Covance; catalog #MMS-101P; 1:100 dilution) by incubating overnight in the humidified chamber (4°C), followed by treatment with a chicken anti-mouse Alexa Fluor 555 secondary antibody (Life Technologies; catalog #A-21200; 1:500 dilution) for 1 h at room temperature. Cells were then permeabilized with 0.01% Triton X (Fisher) and blocked with 1% BSA again, and intracellular SK2 channels were labeled with anti-HA antibody (1:250 dilution) at 4°C overnight and a rabbit anti-mouse Alexa Fluor 633 secondary antibody (Life Technologies; catalog #21427; 1:500 dilution). Coverslips were mounted using mounting medium containing 4′,6-diamidino-2-phenylindole (VectaMount; Vector Laboratories, Inc.; catalog #H-5000) and imaged under a Zeiss LSM 700 confocal laser scanning microscope.

A fluorescence ratio of 555/633 then represents the ratio of SK2 channel numbers on cell membranes over those inside the cells, as we previously described (Rafizadeh et al., 2014). Cells cotransfected with CaM_{WT} or mutant forms of CaM were immunolabeled in parallel, and all the microscopic settings were kept constant for all groups. Blind analysis was performed on unaltered images using Fiji ImageJ.

hiPSC-CMs

Feeder-free hiPSCs (iPS-D19-9-T7; WiCell) were cultured with mTeSR™ on hiPSC-qualified Matrigel. hiPSCs were differentiated into hiPSC-CMs following the protocols we previously reported (Sirish et al., 2016; Yamoah et al., 2018). We have observed ∼80–90% cardiomyocytes as shown previously (Yamoah et al., 2018). The hiPSC-CMs at day 40 (maturing cardiomyocytes) were used for experiments. CaM_{WT} and mutant CaM peptides were used to test the functional changes of endogenous SK currents in hiPSC-CMs. The effects of WT compared with mutant CaMs were tested on the apamin-sensitive currents.

Generation of recombinant CaM proteins

WT and mutant CaM proteins were prepared as previously described (Hwang et al., 2014). Briefly, the recombinant CaM cDNA subcloned into a pET15b vector was mutated using QuikChange site-directed mutagenesis (Agilent Technologies). Proteins were expressed in *Escherichia coli* BL21 (DE3) cells and purified by hydrophobic chromatography using a phenyl sepharose column. Purified protein was dialyzed overnight at 4°C twice in 50 mM HEPES at pH 7.4, 100 mM KCl, and 5 mM EGTA and twice more with the same buffer except EGTA was lowered to 0.05 mM to remove Ca^{2+}. The molecular mass of all proteins was confirmed using negative electrospray mass spectroscopy.

Structural modeling of CaM, CaM mutants, and the hSK2 channel

Structural modeling of CaM_{WT}, CaM_{F90L}, CaM_{F93L}, and CaM_{F142L} and the hSK2 channel was performed using Rosetta loop modeling and relax applications (Bonneau et al., 2001; Rohl et al., 2004; Yarov-Yarovoy et al., 2006; Wang et al., 2007; Yarov-Yarovoy et al., 2012; Bender et al., 2016; Alford et al., 2017) based on the hSK4 bound to the apo-CaM cryo-EM structure (PDB accession no. 6CNM; Lee and MacKinnon, 2018) as a template.

First, we directly compared the sequence between hSK2 (UniProt accession no. Q9H2S1) with the cryo-EM structure of hSK4 (PDB accession no. 6CNM) that was used as the template for molecular modeling. The sequence identity between the two structures is 46%, while the sequence similarity is 63%. We further compared the sequence for the CaMBD (amino acid residues 412–488 in hSK2, DTQLTKRVKNAAANVLRETWLIYKNTKLVKKIDHAKVRKHQRKFLQAIHQLRSVKMEQRKLNDQANTLVDLAKTQNI). The sequence identity between the two CaMBDs is 47% with a sequence identity of 68%.

Downloaded from http://rupress.org/jgp/article-pdf/152/12/e202012667/1800962/jgp_202012667.pdf by guest on 07 February 2026

The hSK2 channel sequence was threaded onto the hSK4 structure. 1,000 models of the hSK2 channel were generated using the Rosetta relax application and then clustered; the top model after clustering was selected as the best hSK2 model. The hSK2 model was used to replace the hSK4 peptide in the CaMBD based on hSK4–CaM complex structure (Lee and MacKinnon, 2018). 1,000 models of the hSK2–CaM complex were generated using the Rosetta relax application and then clustered, and the top model after clustering was selected as the best hSK2-CaM complex model, shown in Fig. 6. To determine the structure of the C-lobe of apo-CaM, CaM was taken from the 6CNM structure, mutated for the mutant models, relaxed, and finally clustered with the top models shown in Fig. 6. The mutant CaM models were created by mutating CaM_{WT} and then using the Rosetta relax application to model potential conformational changes, induced by specific CaM mutations. 10,000 models were generated, the 1,000 lowest energy models were clustered, and the top models after clustering for each CaM mutant were selected as the best model. Molecular graphics and analyses were performed with the University of California San Francisco (UCSF) Chimera package (Pettersen et al., 2004).

MD simulations of WT and mutant CaM

Structures representing WT and mutant apo-CaM were obtained from Rosetta modeling as described above. The webserver CHARMM-GUI was used to prepare apo-CaM and create the solvent box (Jo et al., 2008; Brooks et al., 2009; Lee et al., 2016). The protein was immersed in a TIP3 water box with dimensions of 9 nm on all sides. Na and Cl ions were added to a final concentration of 150 mM to neutralize charge. In total, the system was composed of ∼15,000 (±1,000) atoms (Jo et al., 2008; Brooks et al., 2009; Lee et al., 2016). Periodic boundary conditions with dimensions equivalent to the water box were used (Phillips et al., 2005).

Equilibration and production runs were performed using NAMD 2.13 (Phillips et al., 2005) on a local GPU cluster using CHARMM36m force fields (Vanommeslaeghe et al., 2010; Huang et al., 2017). After 100,000 steps of steepest descent minimization, MD simulations started with a time step of 1 fs, with harmonic restraints initially applied to protein heavy atoms. These restraints were slowly released over 0.5 ns. These systems were equilibrated further for 0.2 ns with a time step of 2 fs. To use a 2-fs time step, all bonds to H atoms were constrained using the SHAKE algorithm. All simulations were performed in isothermal-isobaric ensemble. Temperature was maintained at 303.15 K using a Langevin thermostat, and constant pressure at 1 atm was maintained using a Nosé-Hoover barostat.

Electrostatic interactions were computed using the Particle Mesh Ewald method (Darden et al., 1993). Non-bonded pair lists were updated every 10 steps with a list cutoff distance of 16 Å and a real space cutoff of 12 Å, with energy switching starting at 10 Å. After equilibration of 1 ns, the simulation was continued for 1 µs. The full trajectory, including the equilibration and production steps, was used to calculate the RMSD. The 1-µs trajectory of the simulation during the production step was saved every 0.2 ns. This trajectory was then used for analysis.

RMSD

All measurements and renderings were performed using Visual Molecular Dynamics (Humphrey et al., 1996). RMSD was calculated every 0.2 ns over the equilibration, and production steps aligned to the first frame in the equilibration step. Specifically, for every 0.2 ns of the production simulation, the RMSD was calculated for apo-CaM_{WT} and the mutant CaMs. The structures were clustered, and the cluster with the most decoys was selected as the most probable, with the center of the cluster being used as the representative model. Each mutant CaM structure was aligned individually to the CaM_{WT} representative model using the matchmaker tool in UCSF Chimera, and the distance between the C-α of each residue was calculated. The averaged distance and the SD for each comparison for the full C-terminal domain (residues 81–145) and for Ca^{2+} binding site 4 (residues 131–138) was quantified (Table S1 and Table S2).

Root mean square fluctuation (RMSF)

Per residue RMSF was calculated over a sliding average window of 1 ns time and averaged over the 1-µs trajectory. The per-residue RMSF is presented as mean ± SD.

Ensembles were generated by clustering the MD run as described in the structural modeling section. The top 10 models were displayed and aligned with the top cluster model.

Data analysis

Data analysis from patch-clamp recordings was performed by using Origin software (OriginLab). Current density obtained from cells expressing SK2 with CaM_{WT} or mutant CaM was compared by normalizing the currents with cell capacitance. Where appropriate, pooled data are presented as means ± SEM. Statistical comparisons were performed using one-way and two-way ANOVA combined with Tukey's post hoc analyses. One-way ANOVA was used to determine statistically significant differences among three or more groups in Fig. 1, Fig. 2, Fig. 4, and Fig. 5. Two-way ANOVA was used to determine statistically significant differences with two independent variables among three or more groups in Fig. 3. Post hoc analyses were performed using Tukey's test. Statistical analyses were performed using GraphPad Prism and Origin Software.

Online supplemental material

Fig. S1 shows summary data for fluorescence intensity under NP (left bars) and permeabilized (right bars) conditions for HEK 293 cells expressing SK2 fusion protein with HA tag coexpressed with CaM_{WT} or mutant CaMs (N54I, F90L, D96V, N98S, and D130G). Fig. S2 shows RMSD graphs that include the equilibration and production stages. Fig. S3 shows the top 10 clustered models of apo-CaM_{F90L}, apo-CaM_{F93L}, and apo-CaM_{F142L} aligned to represent an ensemble of possible states, illustrating the distribution of helix 3 and Ca^{2+}-binding site 4 regions. Fig. S4 presents graphical comparisons from MD simulations of the C-lobe of apo-CaMs showing hydrogen bond in the apo-CaM_{WT}. The side chain of Asn^{112} on helix 2 in apo-CaM_{WT} maintains a stable hydrogen bond with the carboxyl oxygen of Ala^{89} residue on helix 1 during simulations of apo-CaM_{WT}, which is not observed in the simulations of the CaM mutants. Fig. S5 shows comparison of the RMSF of Ca^{2+}-CaM_{F142L} from MD simulations

Downloaded from http://rupress.org/jgp/article-pdf/152/12/e202012667/1800962/jgp_202012667.pdf by guest on 07 February 2026

(A) and N-H heteronuclear NOE saturated/unsaturated ratio (B; BMRB: 34262; Wang et al., 2018), with similar flexibility including identification of the most flexible amino acid being Lys^{116} residue. Video 1, Video 2, and Video 3 show morph videos from the top Rosetta model of the C-lobe of apo-CaM_{WT} to the top Rosetta models of apo-CaM_{F90L}, apo-CaM_{F93L}, and apo-CaM_{F142L}, respectively. Video 4, Video 5, and Video 6 show morph videos from the top MD model of the C-lobe of apo-CaM_{WT} to the top MD models of apo-CaM_{F90L}, apo-CaM_{F93L}, and apo-CaM_{F142L}, respectively. Table S1 shows quantification of the RMSD calculated from the production portion of MD presented in Fig. S2. Table S2 shows quantification of the differences in the RMSD among WT and mutant CaMs, derived from the C-terminal domain (residues 81–145) and Ca^{2+} binding site 4 (residues 131–138) presented in Fig. 8.

Results

Inhibitory effects of human CaM mutations on SK channels

We first coexpressed human cardiac SK2 channels with different human mutant CaMs compared with CaM_{WT} in HEK 293 cells. Our previous studies showed that cytoskeletal proteins are critical for the proper membrane localization of SK2 channels; therefore, α-actinin2 and FLNA were also used for coexpression in all groups (Lu et al., 2009; Rafizadeh et al., 2014; Zhang et al., 2017).

As positive controls, we tested the roles of the N- and C-lobe mutant CaMs in the regulation of SK2 currents using $CaM_{1,2}$ and $CaM_{3,4}$, where the two Ca^{2+}-binding sites in the N- and C-lobe are mutated, respectively, as well as a mutant CaM ($CaM_{1,2,3,4}$) that abolishes the four high affinity Ca^{2+}-binding sites (Xia et al., 1998). Apamin-sensitive $I_{K,Ca}$ is recorded at baseline (before apamin application, black traces) and after apamin application (10 nM, red traces, Fig. 1 A). Both EF hands in the N- and C-lobe of CaM play critical roles in activation of the apamin-sensitive current (Fig. 1 A). Moreover, $CaM_{1,2,3,4}$ results in the most significant inhibition on the apamin-sensitive current compared with $CaM_{1,2}$ and $CaM_{3,4}$ (Fig. 1 A). Summary data for the density of apamin-sensitive currents at the test potentials of −120 and +60 mV are shown in Fig. 1 B. The results are distinct from those previously reported demonstrating the critical roles of Ca^{2+} binding to the N- but not the C-lobe of CaM in SK channel gating in oocytes (Keen et al., 1999). However, our experiments were performed in a mammalian expression system with coexpression of α-actinin2 and FLNA. Furthermore, our previous study documented binding of α-actinin2 to the CaMBD of SK2 channels (Lu et al., 2007; Lu et al., 2009; Rafizadeh et al., 2014).

Next, we tested the effects of LQTS (CaM_{D96V}, CaM_{D130G}), CPVT (CaM_{N54I}, CaM_{N98S}), and IVF (CaM_{F90L}) CaM mutants compared with CaM_{WT}. Fig. 1 C shows the most prominent inhibitory effects on the density of apamin-sensitive currents by the two LQTS mutations (CaM_{D96V} and CaM_{D130G}). CaM_{F90L} resulted in the least inhibitory effects. The current densities at −120 mV and +60 mV are shown in Fig. 1 D.

No significant alteration in SK2 channel trafficking by human mutant CaMs

The effects of CaM mutations on SK2 current may result from a decrease in channel activation or trafficking to the cell membrane. We therefore tested if the reduction in the SK2 current density from coexpression of mutant CaMs results from a decrease in membrane trafficking. Immunofluorescence confocal microscopy was performed using SK2 channels harboring an HA tag in the extracellular S1-S2 loop (SK2-HA) by using NP compared with permeabilized (P) conditions as we previously described (Fig. 2 and Fig. S1; Rafizadeh et al., 2014). Our data suggest that the mutant CaM does not alter SK channel trafficking.

Inhibitory effects of mutant CaMs on SK2 channels revealed by SK2 fusion protein harboring CaM_{WT} or mutant CaMs via a flexible glycine (G_n) linker

There are some possible caveats inherent in the experiments presented in Fig. 1 since mutations in CaMs may alter the efficiency of CaM expression in HEK 293 cells. To circumvent these possible confounding factors, we generated SK2 channel fusion constructs harboring CaM_{WT} (hSK2-G_4-CaM_{WT}) or mutant CaMs (hSK2-G_4-CaM_{MUT}) to specifically occupy the CaMBD of SK2 channels with CaM_{WT} or mutant CaMs using flexible linkers (G_n linker; Fig. 3 A), as previously described by Mori et al. (2004). This experimental paradigm enabled us to selectively test the contribution of the mutant CaMs compared with that of CaM_{WT} on SK2 channels (Fig. 3 A).

We first demonstrated that the fusion proteins behave as expected by directly comparing apamin-sensitive $I_{K,Ca}$ recorded from HEK 293 cells expressing hSK2-G_4-CaM_{WT} versus hSK2 coexpressed with CaM_{WT} (Fig. 3, B and C). Furthermore, coexpression of DN CaM ($CaM_{1,2,3,4}$) with hSK2-G_4-CaM_{WT} failed to knock down apamin-sensitive current (Fig. 3, B and C) in contrast to hSK2 coexpressed with $CaM_{1,2,3,4}$, as shown in Fig. 1 A.

Having determined that the fusion proteins function as expected, we compared the density of apamin-sensitive currents between hSK2-G_4-CaM_{MUT} and coexpression of the SK2 channel and mutant CaMs. The density is comparable, with the most significant inhibitory effects on $I_{K,Ca}$ by the two LQTS mutations tested (CaM_{D96V} and CaM_{D130G}), consistent with a DN effect from these mutations (Fig. 3, D and E). We further tested the effects of two additional mutant CaMs (F93L and F142L). CaM_{F142L} is shown to be linked to LQTS, while the Phe^{93} residue is predicted from our molecular model to interact with CaMBD of SK2 channels (described in a later section). These two mutations produced intermediate effects on $I_{K,Ca}$ (Fig. 3, D and E).

Functional effects of mutant CaMs on SK currents in hiPSC-CMs

Thus far, the experiments have relied on a heterologous expression system. We took advantage of hiPSC-CMs. The rationale was to determine the functional effects of mutant CaMs on endogenous SK currents with accompanying ion channel interacting proteins within a human cardiomyocyte-like cell. Even though hiPSC-CMs are relatively immature, we demonstrated the expression of SK2 channels in hiPSC-CMs using immunofluorescence confocal microscopy (Fig. 4 A). Fig. 4 B shows apamin-sensitive current in hiPSC-CMs when the cells were dialyzed by WT or mutant CaM proteins. Dialysis of mutant CaM_{D96V} proteins resulted in the most prominent knockdown of apamin-sensitive currents in hiPSC-CMs,

Downloaded from http://rupress.org/jgp/article-pdf/152/12/e202012667/1800962/jgp_202012667.pdf by guest on 07 February 2026

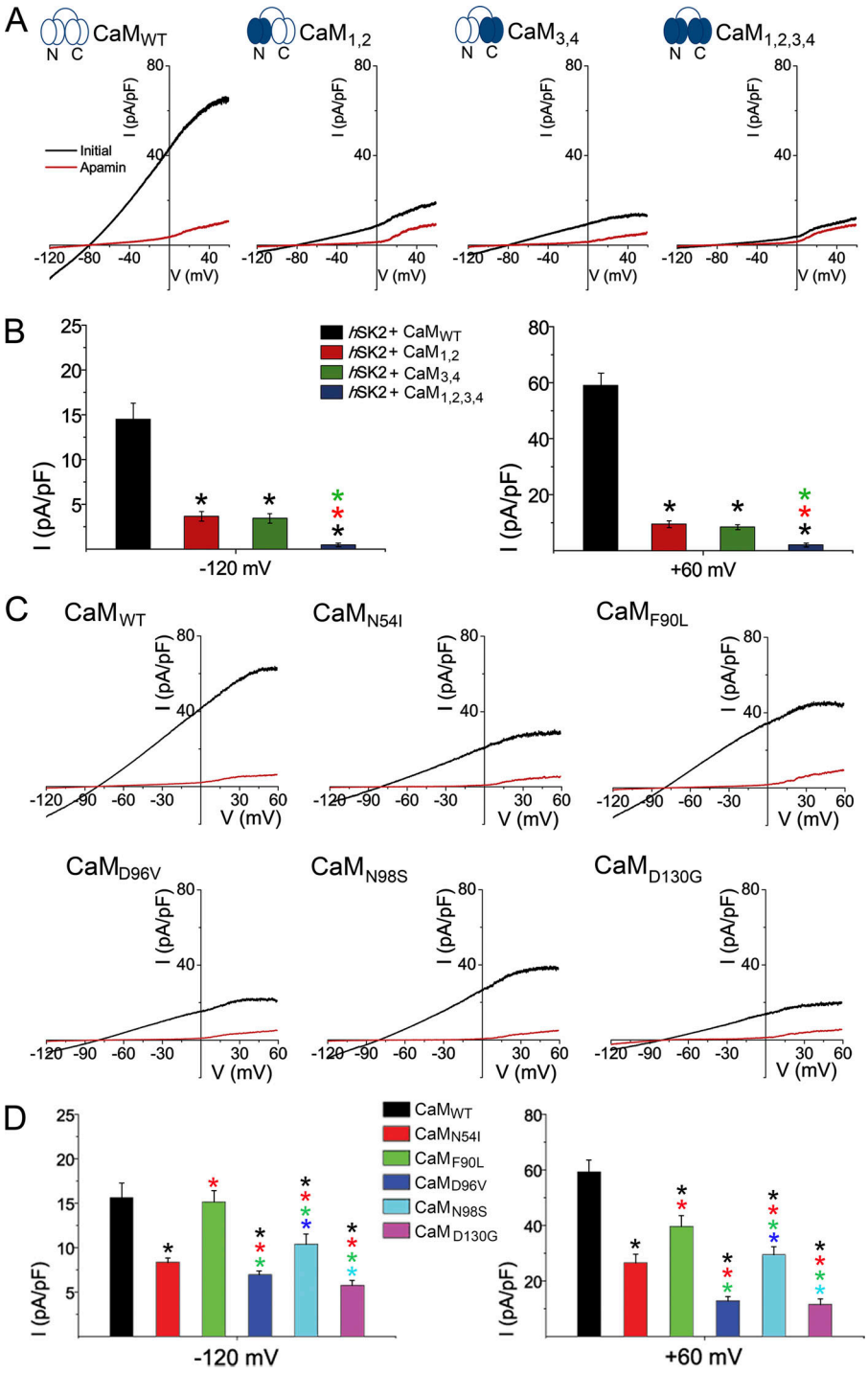

Figure 1. **Mutations in the N-lobe and C-lobe of CaM affect the currents of hSK2 expressed in HEK 293 cells. (A)** hSK2 channels were coexpressed with CaM_{WT} or mutant CaMs ($CaM_{1,2}$, $CaM_{3,4}$, or $CaM_{1,2,3,4}$). Current was recorded before (black trace) and after (red trace) application of apamin (10 nM). **(B)** Summary data at +60 and −120 mV indicating significant reduction of the SK currents by mutant CaMs (n = 12 cells; *, P < 0.05). **(C and D)** hSK2 channels were coexpressed with CaM_{WT} (black bars), CaM_{N54I} (red bars), CaM_{F90L} (green bars), CaM_{D96V} (blue bars), CaM_{N98S} (cyan bars), and CaM_{D130G} (magenta bars). **(C)** Current was recorded before (black trace) and after (red trace) application of apamin (10 nM). **(D)** Summary data at −120 mV and +60 mV (n = 10–13 cells; *, P < 0.05). For B and D, the colors of the asterisks denote comparisons with the corresponding bar graphs of the same colors, using one-way ANOVA combined with Tukey's test (at −120 mV, P = 0.00001 for all pairwise comparisons except P = 0.04 for CaM_{N54I} versus CaM_{D96V}, and P = NS for CaM_{D96V} versus CaM_{D130G} and CaM_{WT} versus CaM_{F90L}; at +60 mV, P = 0.00001 for all pairwise comparisons except P = NS for CaM_{D96V} versus CaM_{D130G}). Data shown represents mean ± SEM.

consistent with its DN effects, compared with the effects of CaM_{F90L} (Fig. 4, C and D).

Altered interaction between the SK2 channel and mutant CaMs

Coimmunoprecipitation was performed as we previously described (Lu et al., 2007) between SK2-HA channels (Fig. 5 A) and different mutant CaMs compared with CaM_{WT}. Since native cells contain a large amount of CaM, we constructed a fusion protein of CaM with FLAG-tag (DYKDDDDK; CaM_{FLAG}) to enable identification of transfected mutant CaMs versus endogenous CaM_{WT} (Fig. 5 B). There was a significant decrease in SK2 channels complexed with mutant CaM_{F90L} in the absence of Ca^{2+} with EGTA (Fig. 5 C). Negative control experiments were performed using nontransfected cells and cells transfected with SK2-HA alone, without CaM_{FLAG}. The data suggest a significant reduction in SK2 channel complexed with apo-CaM_{F90L} compared with other CaM mutants, supporting the lack of DN effects with relatively modest inhibition of CaM_{F90L} on SK2 currents.

Downloaded from http://rupress.org/jgp/article-pdf/152/12/e202012667/1800962/jgp_202012667.pdf by guest on 07 February 2026

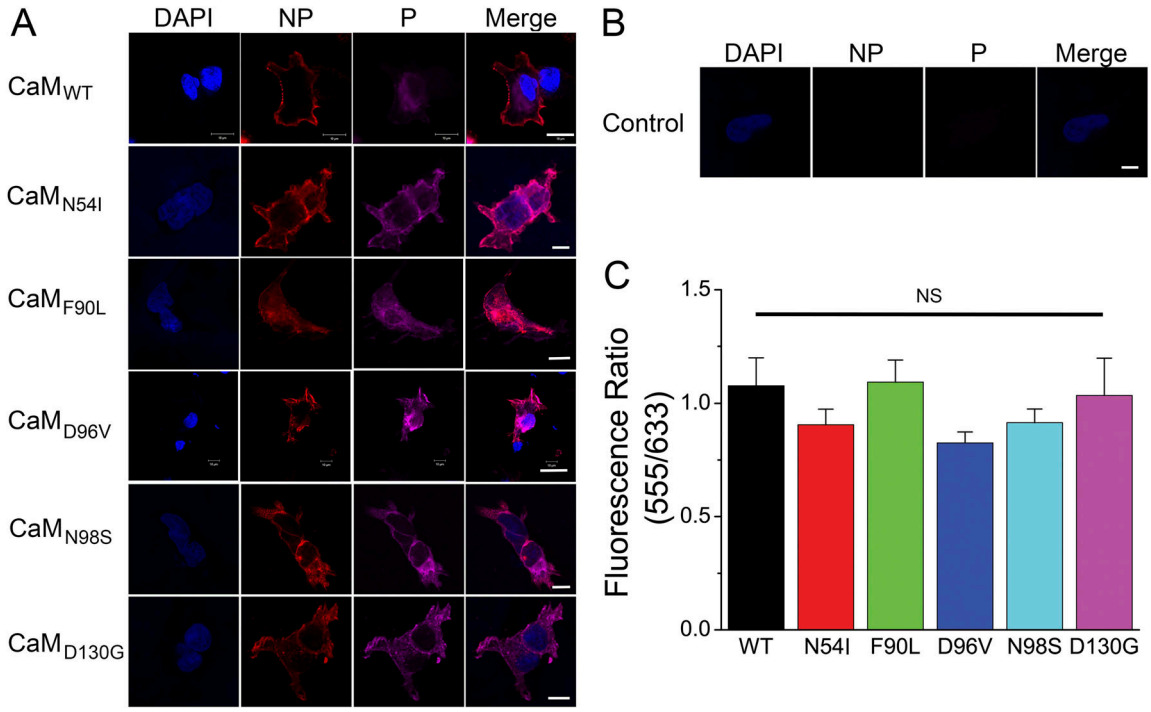

Figure 2. **Trafficking of hSK2 channels after coexpression with CaM_{WT} or mutant CaMs. (A)** HEK 293 cells expressing SK2 fusion protein with HA tag coexpressed with CaM_{WT} or mutant CaMs (N54I, F90L, D96V, N98S, and D130G) using NP and permeabilized (P) conditions. **(B)** Control represents incubation with secondary antibody alone. Scale bars are 10 µm. **(C)** Summary data showing fluorescence intensity under NP/P conditions (555/633 fluorescent intensity). Data shown represent mean ± SEM. Statistical analyses were performed using one-way ANOVA combined with Tukey's test. *n* = 15–20 cells; P = NS. DAPI, 4′,6-diamidino-2-phenylindole.

Structural modeling of CaM_{F90L}, CaM_{F93L}, and CaM_{F142L} mutants and their interactions with SK2 channels

To explore potential structural changes induced by CaM mutations, we generated structural models of the C-lobe of apo-CaM_{WT}, apo-CaM_{F90L}, apo-CaM_{F93L}, and apo-CaM_{F142L} using Rosetta structural modeling. The models of CaM reveal that Phe → Leu mutations resulted in conformational changes that affected helix packing in the C-lobe due to the substitution of a relatively large phenylalanine side chain to a smaller leucine side chain (Fig. 6, B–D). The Phe^{90} side chain is surrounded by the following residues in apo-CaM_{WT}: Arg^{87} in helix 1; Ile^{101} in loop 1–2; Val^{137} in loop 3–4; and Tyr^{139} and Phe^{142} in helix 4. The Phe^{93} side chain is surrounded by the following residues in apo-CaM_{WT}: Ile^{101} in loop 1–2; Leu^{106} and Val^{109} in helix 2; and Phe^{142}, Met^{145}, and Met^{146} in helix 4. The Phe^{142} side chain is surrounded by the following residues in apo-CaM_{WT}: Ile^{86}, Phe^{90}, and Phe^{93} in helix 1; Ile^{101} in loop 1–2 and Leu^{106} in helix 2; Val^{137} in loop 3–4; and Tyr^{139}, Met^{145}, and Met^{146} in helix 4. Notably, Phe^{90}, Phe^{93}, and Phe^{142} are interacting with each other in apo-CaM_{WT}. The conformational effects of the Phe → Leu mutations are explored in more detail using MD simulations.

Additionally, we generated a structural model of apo-CaM_{WT} in complex with CaMBD from the SK2 channel based on the cryo-EM structure of the SK4 channel in complex with apo-CaM (PDB accession no. 6CNM; Lee and MacKinnon, 2018). The three phenylalanine residues (Phe^{90}, Phe^{93}, and Phe^{142}) from the C-lobe of CaM can be seen interacting with hydrophobic residues from the CaMBD of SK2 channels (Fig. 6, E and F). Consistent with our hypothesis and the coimmunoprecipitation study (Fig. 5), we predict that substitution of the phenylalanine side chain may result in a significant decrease in the interaction of apo-CaM and SK2 CaMBD. Even though CaM_{F90L} and CaM_{F142L} were previously described to be linked to human arrhythmias, CaM_{F93L} has not been described in patients. Our molecular modeling predicts that the Phe^{93} residue intimately interacts with SK2 CaMBD. Indeed, CaM_{F93L} results in a significant decrease in SK2 current, supported by our functional analyses (Fig. 3, D and E).

MD simulations provide insights into the conformational changes of CaM_{F90L}, CaM_{F93L}, and CaM_{F142L}

To further explore potential conformational changes induced by the Phe → Leu mutations in CaM, we performed MD simulations on the WT and three CaM mutants: F90L, F93L, and F142L. Each simulation was performed for 1 µs after equilibration. The simulation for apo-CaM_{WT} was performed twice. The RMSDs demonstrated that the system equilibrated rapidly and that the RMSD had plateaued for the entire runs (Fig. S2 and Table S1).

Analyses of the RMSF show remarkable findings that the three Phe → Leu mutants affected the per-residue structure in similar manners (Fig. 7), even though the mutants are located in different helices of the C-lobe of CaM (helix 1 contains Phe^{90} and Phe^{93}, and helix 4 contains Phe^{142}). Compared with apo-CaM_{WT} from the first simulation, all three CaM mutants exhibited more flexibility toward the C-terminal end of helix 2, while the C-terminal end of helix 3 and Ca^{2+}-binding site 4 were less

Downloaded from http://rupress.org/jgp/article-pdf/152/12/e202012667/1800962/jgp_202012667.pdf by guest on 07 February 2026

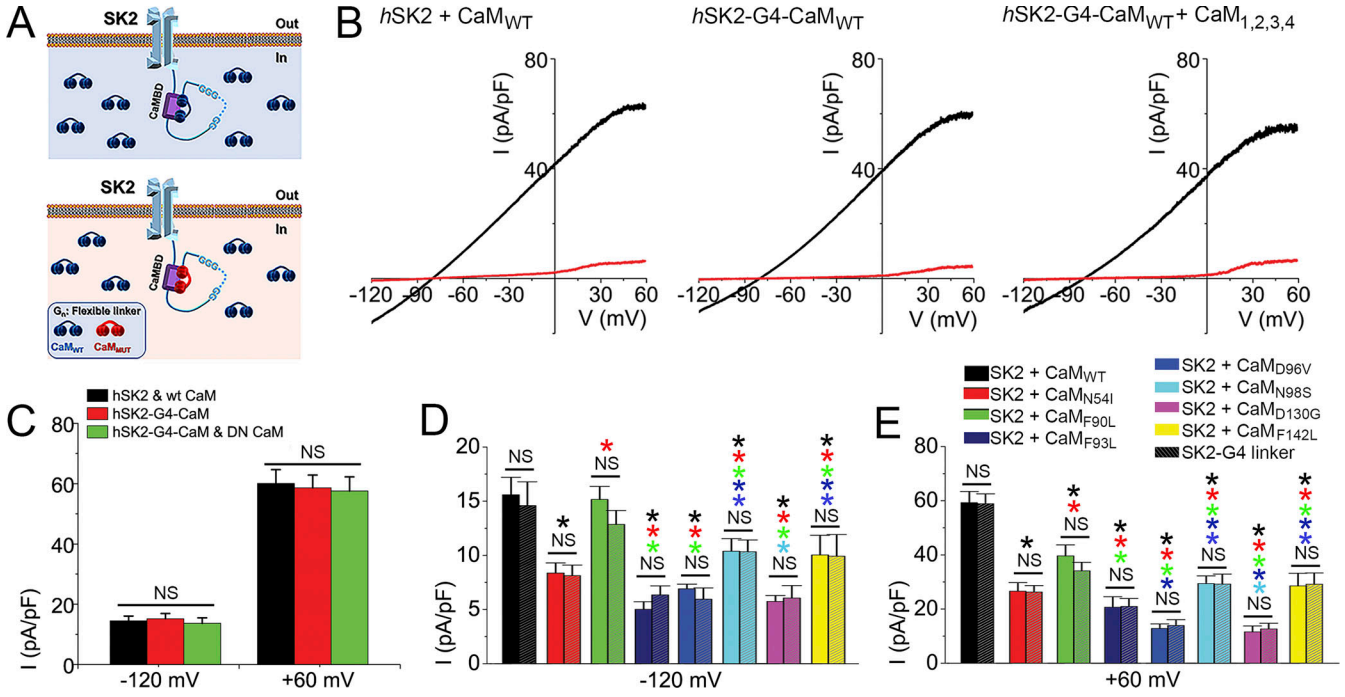

Figure 3. **hSK2-CaM fusion proteins exhibit similar inhibitory effects to that of coexpressed hSK2 channels with CaM. (A)** Diagram illustrating experimental paradigms using SK2 fusion proteins with flexible G_n linker fused to CaM_{WT} (upper panel) compared with mutant CaMs (lower panel). **(B)** Current recordings before (black trace) and after (red trace) apamin application (10 nM) for hSK2 expressed with CaM_{WT} versus hSK2-G4-CaM_{WT} versus SK2-G4-CaM_{WT} expressed with DN $CaM_{1,2,3,4}$. **(C)** Summary data at −120 mV and +60 mV from B. **(D and E)** Summary data for apamin-sensitive current density in HEK 293 cells coexpressing hSK2 with CaM_{WT} or mutant CaM constructs (left bars) compared with SK2-G4-CaM_{WT} or SK2-G4-CaM_{MUT} (hashed bars on the right), where CaM_{MUT} refers to CaM_{N54I} (red bars), CaM_{F90L} (green bars), CaM_{F93L} (purple bars), CaM_{D96V} (blue bars), CaM_{N98S} (cyan bars), CaM_{D130G} (magenta bars), and CaM_{F142L} (yellow bars) at −120 mV (D) and +60 mV (E; *n* = 10–13 cells). Data represent mean ± SEM. Statistical analysis was performed using two-way ANOVA combined with Tukey's test. The colors of the asterisks denote comparisons with the corresponding bar graphs of the same colors. *, $P < 0.05$. At −120 mV, $P = 0.00001$ for all pairwise comparisons except $P = 0.04$ for CaM_{N54I} versus CaM_{F93L} and CaM_{N54I} versus CaM_{D96V}, and P = NS for CaM_{WT} versus CaM_{F90L}, CaM_{F93L} versus CaM_{D96V}, CaM_{F93L} versus CaM_{D130G}, CaM_{D96V} versus CaM_{D130G}, and CaM_{N98S} versus CaM_{F142L}. At +60 mV, $P = 0.00001$ for all pairwise comparisons except P = NS for CaM_{D96V} versus CaM_{D130G} and CaM_{N98S} versus CaM_{F142L}. There were no significant differences between hSK2 coexpression with CaM compared with hSK2-G4-CaM for WT or mutant CaMs (P = NS).

flexible. The largest shifts in RMSF were observed where the side chains of Phe^{90}, Phe^{93}, and Phe^{142} contact helices 2 and 3. This agrees with the notion that the Phe → Leu mutation creates a void volume, allowing helices 2 and 3 to repack their side chains and readjust their backbone positions (Fig. 8, Fig. S3, Video 1, Video 2, Video 3, Video 4, Video 5, and Video 6). Differences in the RMSD between an equilibrated apo-CaM_{WT} and mutant CaMs shown in Fig. 8 are quantified for the C-terminal domains as well as for Ca^{2+}-binding site 4 (Table S2).

The RMSD from Simulation 2 of the apo-CaM_{WT} exhibited a transient increase before returning to baseline toward the end of the simulation (Fig. S2). Closer examinations revealed that the major contributing regions of apo-CaM_{WT} toward the transient increase in the RMSD in Simulation 2 are in helix 3, just proximal to Ca^{2+}-binding site 4, similar to the conformational changes we observed in Simulation 1 but at a larger magnitude. Additionally, Simulation 2 of apo-CaM_{WT} exhibited a similar per-residue RMSF pattern to Simulation 1, albeit lower in magnitude, as demonstrated in Fig. 7. This is consistent with the lower value of RMSD for Simulation 2 compared with Simulation 1 for the majority of the run. Finally, there was a return to the average RMSD after the transient increase, supporting the equilibration of the simulations.

Consistent with our observation, the side chain of Asn^{112} on helix 2 in apo-CaM_{WT} maintained a stable hydrogen bond with the carboxyl oxygen of the Ala^{89} residue on helix 1 during the simulations of the apo-CaM_{WT}, which was not observed in the simulations of the CaM mutants (Fig. S4). This may also, in part, influence flexibility toward the C-terminal end of helix 2 of the three mutant CaMs, as discussed above. We suggest that these observed changes may result in a decrease in the interaction of apo-CaM and SK2 CaMBD. Finally, to validate the MD simulations, we directly compared RMSF of Ca^{2+}-CaM_{F142L} from the MD simulation with the publicly available N-H heteronuclear NOE saturated/unsaturated ratio from a previously published NMR structure (BMRB accession no. 34262; Wang et al., 2018). Indeed, there is significant similarity in flexibility, including identification of the most flexible amino acid residue as Lys^{116} (Fig. S5).

Discussion

The gating of SK channels relies on Ca^{2+} binding to CaM. Therefore, mutations of CaM in human calmodulinopathy are predicted to have significant effects on SK channel function. In the current study, we demonstrate a significant reduction in SK

Downloaded from http://rupress.org/jgp/article-pdf/152/12/e202012667/1800962/jgp_202012667.pdf by guest on 07 February 2026

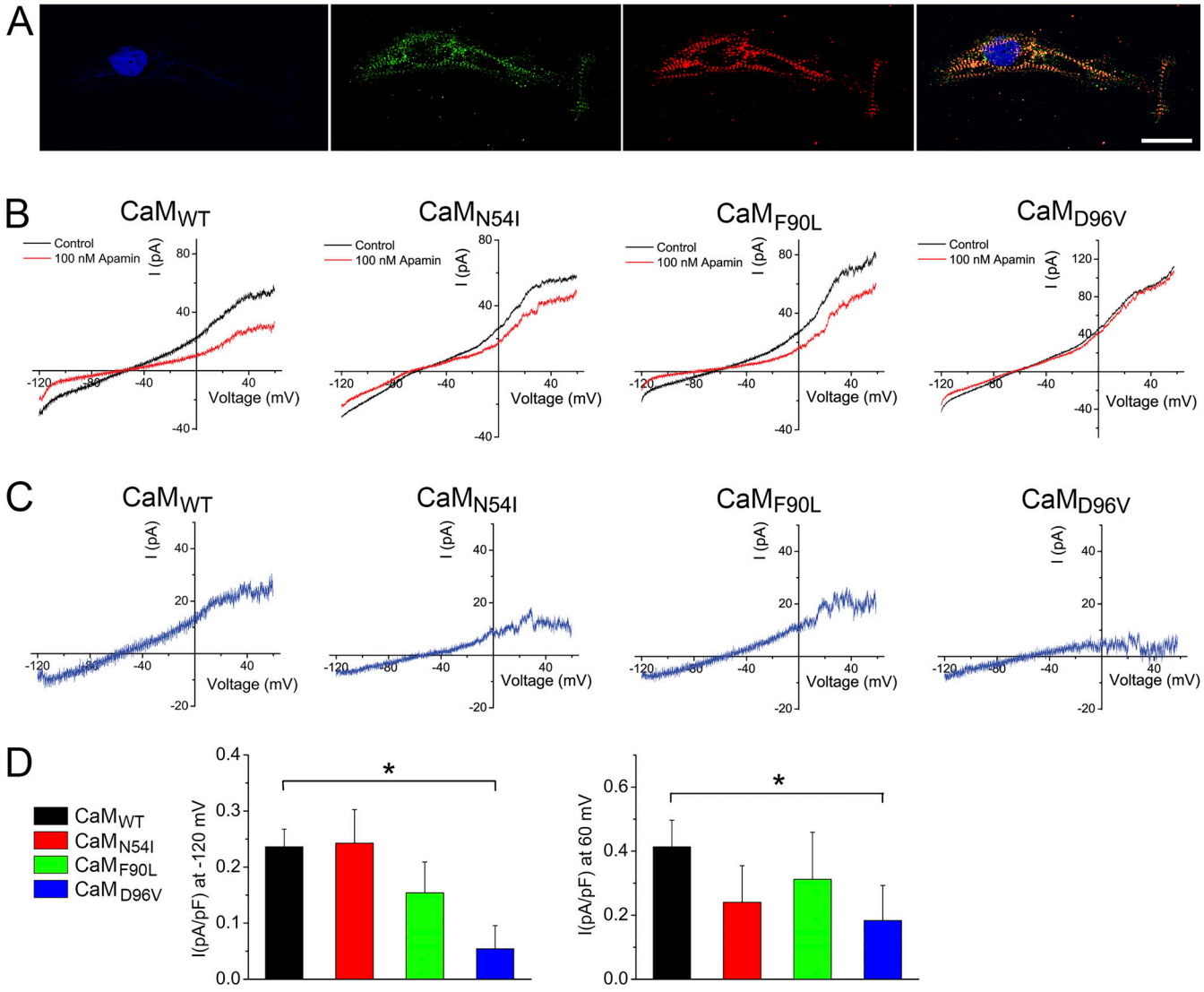

Figure 4. **Regulation of endogenous SK currents in hiPSC-CMs by intracellular CaM peptides. (A)** hiPSC-CMs expressing SK2 channels (green) and α-actinin2 (red). 4′,6-Diamidino-2-phenylindole stain is shown in blue. Scale bar is 10 µm. **(B)** Effects of mutant CaM peptides (CaM_{N54I}, CaM_{F90L}, and CaM_{D96V}) compared with CaM_{WT} peptide on apamin-sensitive SK currents in hiPSC-CMs. The current was recorded before (black trace) and after (red trace) apamin application (100 nM). **(C)** Subtracted apamin-sensitive SK currents in the presence of CaM_{WT} and mutant CaM peptides. **(D)** Comparisons of the apamin-sensitive current densities at −120 mV and +60 mV (n = 8–10 cells). Data represent mean ± SEM. Statistical analyses were performed using one-way ANOVA combined with Tukey's test; *, P = 0.012 at −120 mV, and *, P = 0.037 at +60 mV between CaM_{WT} and CaM_{D96V}.

currents in the presence of the LQTS CaM mutants CaM_{D96V} and CaM_{D130G}. The marked reduction in SK currents in the presence of LQTS CaM mutants is consistent with their DN effects. Immunofluorescence staining does not show significant changes in membrane-bound SK2 channels in the presence of WT or mutant CaM, suggesting that the effects of these CaM mutants are primarily on the Ca^{2+}-CaM–dependent activation of the channels. The DN effect is predicted to result in a reduction in repolarization reserve. We confirmed these results using tandem SK2-CaM constructs to circumvent potential caveats from endogenous CaM in HEK 293 cells and/or changes in CaM expression from mutant constructs.

In contrast to the marked DN effects of CaM_{D96V} and CaM_{D130G}, CaM_{F90L} results in only a modest reduction in $I_{K,Ca}$, suggesting a distinct mechanism by disrupting the interaction between apo-CaM and the SK channel without the DN effects. Structural modeling and MD simulations reveals the atomistic mechanisms in conformational changes caused by the phenylalanine-to-leucine mutation, which affect helix packing in the C-lobe, disrupting interactions between apo-CaM with CaMBD of SK channels.

In Fig. 1, we showed that CaM_{D96V} exhibits the most prominent inhibitory effect, while CaM_{F90L} exerts only a mild inhibitory effect on apamin-sensitive current. Consistently, dialysis of mutant CaM_{D96V} proteins in hiPSC-CMs results in the most prominent knockdown of apamin-sensitive currents in hiPSC-CMs compared with CaM_{F90L} (Fig. 4). As expected, the endogenous SK currents in hiPSC-CMs (Fig. 4) are much smaller than the overexpressed SK currents in HEK 293 cells (Fig. 1). Therefore, the two systems were used as complementary studies to evaluate the effects of CaM mutants on SK currents.

Downloaded from http://rupress.org/jgp/article-pdf/152/12/e202012667/1800962/jgp_202012667.pdf by guest on 07 February 2026

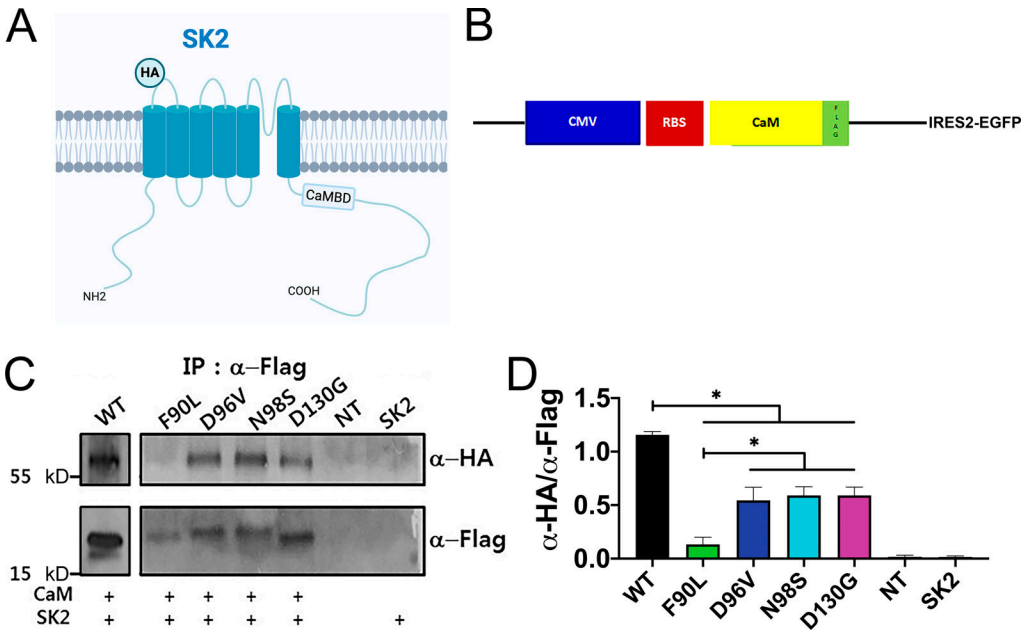

Figure 5. **Interactions of mutant CaMs with SK2 channels revealed by coimmunoprecipitation assay. (A and B)** Diagrams depicting the SK2 channel subunit with an HA tag in the S1-S2 extracellular loop and CaM with a FLAG tag in the C terminus under the cytomegalovirus (CMV) promoter. RBS, ribosome-binding site. **(C)** Coimmunoprecipitation using anti-Flag antibody (α-Flag) to pull down SK2 channels identified using anti–HA antibody (α-HA) in the presence of 2 mM EGTA. The right two lanes show the results from nontransfected HEK 293 cells (NT) and cells transfected with SK2 channels only (SK2) as negative controls. **(D)** Summary data of the findings in C. The background subtracted intensity for SK2 bands using anti–HA antibody was normalized to CaM bands using anti-Flag antibody (NIH ImageJ). Data shown represent mean ± SEM (n = 3). Statistical analyses were performed using one-way ANOVA combined with Tukey's test; *, P < 0.05 for CaM_{WT} compared with CaM_{F90L}, CaM_{D96V}, CaM_{N98S}, and CaM_{D130G}, and *, P < 0.05 for CaM_{F90L} compared with CaM_{D96V}, CaM_{N98S}, and CaM_{D130G} (the P values are as follows: CaM_{WT} versus CaM_{F90L}, 0.00003; CaM_{WT} versus CaM_{D96V}, 0.002; CaM_{WT} versus CaM_{N98S}, 0.004; CaM_{WT} versus CaM_{D130G}, 0.004; CaM_{F90L} versus CaM_{D96V}, 0.03; CaM_{F90L} versus CaM_{N98S}, 0.02; and CaM_{F90L} versus CaM_{D130G}, 0.02). IP, immunoprecipitation.

There are six CaM alleles, and a mutation in one allele is expected to have only a partial effect on the overall CaM pool within the cell. Therefore, other possible mechanisms may play a role, including cell-specific differential expression of the different alleles.

Mechanisms of human calmodulinopathy

CaM serves as a Ca^{2+} sensor for many ion channels and transporters and consequently has been shown to play key roles in the regulation of cardiac excitability; mutations in CaM have been linked to LQTS, CPVT, and IVF (Crotti et al., 2013; George, 2015; Reed et al., 2015; Boczek et al., 2016). Studies on calmodulinopathy have provided evidence of the critical roles of CaM in the functional regulation of $Ca_v1.2$, RYR2, $K_v7.1$, and SK channels, among others (Nyegaard et al., 2012; Crotti et al., 2013; Fukuda et al., 2014; Hwang et al., 2014; George, 2015; Vassilakopoulou et al., 2015; Yu et al., 2016).

CaM_{D96V} and CaM_{D130G} occur in highly conserved aspartic acid residues responsible for chelating Ca^{2+} ions in the C-lobe (Crotti et al., 2013). Consequently, CaM_{D130G} has been shown to have markedly decreased Ca^{2+}-binding affinity (Hwang et al., 2014; Vassilakopoulou et al., 2015). In addition, CaM_{D130G} was reported to have decreased interaction with RYR2, possibly through a DN effect. CaM_{D96V} was previously shown to exhibit an increased K_d for Ca^{2+} binding compared with CaM_{WT}, although to a lesser extent than CaM_{D130G} (Vassilakopoulou et al., 2015). LQTS mutants (D96V, D130G, and F142L) have been reported to exhibit reduced Ca^{2+} affinity compared with that of CaM_{WT} and CPVT (N54I and N98S) mutants (Hwang et al., 2014). In addition, the LQTS-associated mutants have been shown to suppress CDI of L-type Ca^{2+} currents (Limpitikul et al., 2014).

Potential roles of cardiac SK channels in calmodulinopathy

We previously identified the expression of SK channels (SK1, SK2, and SK3) in the heart and demonstrated the critical roles of the channels in mediating action potential repolarization in human atrial myocytes (Xu et al., 2003; Tuteja et al., 2005). SK2 channels physically coupled to α-actinin2, allowing a close association with LTCCs (Lu et al., 2007, 2009). The subcellular localization of SK channels in close proximity to LTCC and RYR2 provides an immediate Ca^{2+} source (Zhang et al., 2018), which, through binding of Ca^{2+} to CaM, triggers conformational changes to activate SK channels. SK channels may also play important roles in the feedback mechanism by regulating the activities of LTCCs and RYR2 to influence local and global Ca^{2+} signaling.

The roles of SK channels in the heart have been extensively studied in the past decade (Zhang et al., 2015). Single nucleotide polymorphisms of *KCNN* genes encoding for SK channels have been shown to be linked to human atrial fibrillation (AF; Roselli et al., 2018), and SK channels may represent a potential novel therapeutic target against atrial arrhythmias (Diness et al., 2015). Importantly, SK channels participate in the electrical

Downloaded from http://rupress.org/jgp/article-pdf/152/12/e202012667/1800962/jgp_202012667.pdf by guest on 07 February 2026

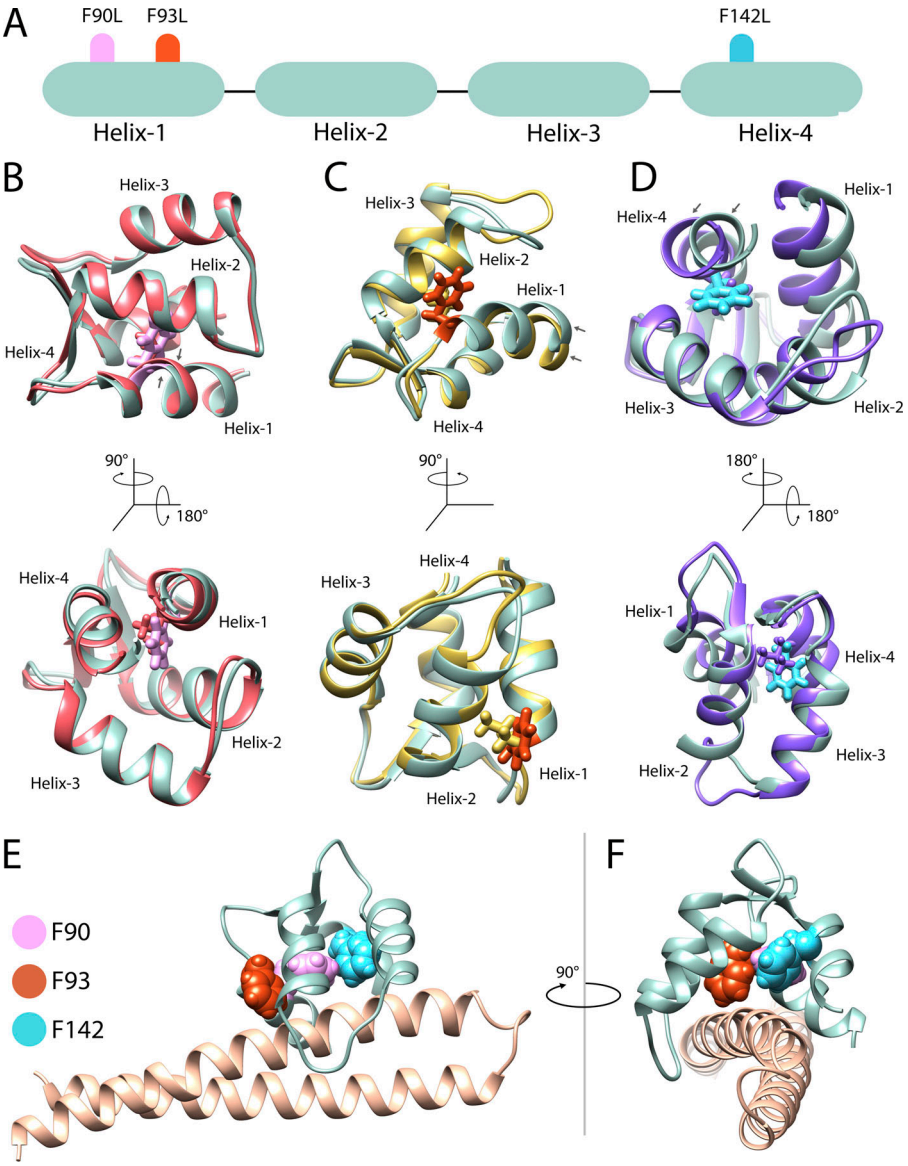

Figure 6. **Structural modeling of the interactions between CaM mutants and SK2 CaMBD. (A)** Schematic of the four α-helices within the C-lobe of CaM. Location of mutations are shown by labels and colored markers. **(B–D)** Comparisons of CaM_{WT} (green) and CaM_{F90L} (red; B), CaM_{F93L} (yellow; C), and CaM_{F142L} (purple; D). Side chains of key amino acid residues are shown in stick representation using the color scheme shown in A. Conformational changes due to CaM mutation are indicated by black arrows in each panel. **(E)** C-lobe of apo-CaM_{WT} (colored in green) bound to the C terminus of hSK2 channel (colored in light brown). Side chains of key amino acids are shown using space-filling representation. **(F)** Panel E rotated 90° to the left around the y axis. Molecular modeling was performed in Ca^{2+}-free conditions.

remodeling in AF and heart failure. SK channels are significantly up-regulated in AF animal models (Ozgen et al., 2007; Qi et al., 2014) and failing ventricular myocytes (Chua et al., 2011; Chang et al., 2013). However, the mechanisms underlying SK channel remodeling in the diseased heart remain unclear.

SK channels are unique because the channels are solely gated by $Ca^{2+}{}_i$ through a highly conserved CaMBD. Our data demonstrate the functional effects, structural basis, and molecular mechanisms of the disease-causing CaM mutants in the regulation of cardiac SK2 channels, highlighting the potential contribution of cardiac SK channels to human calmodulinopathy. Even though SK currents are more prominently expressed in atrial than in ventricular myocytes (Xu et al., 2003; Zhang et al., 2015), SK currents are known to be up-regulated in failing ventricular myocytes (Chua et al., 2011; Chang et al., 2013) and during hypokalemia (Chan et al., 2015). Recent studies have supported their critical roles in cardiac Purkinje cells (Reher et al., 2017), which are known to be the potential site of origin of cardiac arrhythmias, including in patients with heritable arrhythmia syndrome (Haïssaguerre et al., 2002; Wilde et al., 2019). Moreover, SK channels play critical roles in the pacemaker activity of sinoatrial and atrioventricular nodes (Zhang et al., 2008; Torrente et al., 2017). Therefore, mutations in CaMs may result in a significant reduction in the key Ca^{2+}-dependent repolarization currents mediated by SK channels. Even though no SK channel variants have been reported to be associated with an inherited arrhythmia syndrome to date, a recent study reported a rare variant, c.1509C>G (p.F503L), in one *KCNN2* allele in a patient who developed drug-induced LQTS (Ko et al., 2018). Indeed, this is a rapidly expanding area of research.

Additionally, SK2 channels colocalized within microdomains of LTCC and RYR2, which serve as the Ca^{2+} source for the activation of SK channels (Zhang et al., 2018). Activation of SK2 channels provides a direct link between beat-to-beat changes in $Ca^{2+}{}_i$ and membrane potentials, and thus may serve as the feedback mechanisms to regulate the activities of the LTCC and RYR2 channels. Functional effects of CaM mutations on SK channel activation may indirectly

Downloaded from http://rupress.org/jgp/article-pdf/152/12/e202012667/1800962/jgp_202012667.pdf by guest on 07 February 2026

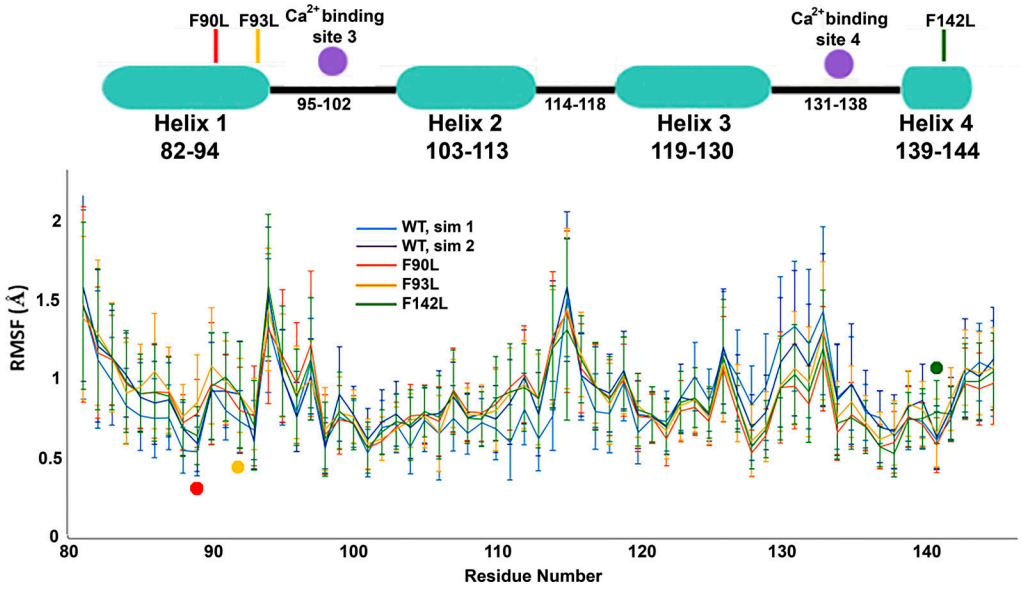

Figure 7. **Graphs of RMSF showing regional changes in stability.** RMSF from MD simulations of the C-lobe of apo-CaM_{WT} is shown in blue (first simulation [sim]) and purple (second simulation), while RMSF from MD simulations of the C-lobe of apo-CaM_{F90L}, apo-CaM_{F93L}, and apo-CaM_{F142L} mutants are shown in red, orange, and green, respectively. Diagrams above the graphs depict helices 1–4 from the C-lobe together with amino acid residues and are scaled to match the residue numbering of the graph. Locations of the three mutations are indicated by their respective colored dot on the graph and bars above the helices. Ca^{2+}-binding sites are indicated with purple dots together with the numbers for the amino acid residues. Data shown are mean ± SD.

disrupt this possible feedback mechanism on LTCC and RYR2 channels.

Recent studies have evaluated the effects of arrhythmogenic CaM mutations on SK2 and SK3 channel function in HEK 293 cells (Yu et al., 2016; Saljic et al., 2019). They similarly observed effects independent of SK2 expression and trafficking; however, our study provides new insights by taking advantage of computational analyses as well as native-like cells through our use of hiPSC-CMs.

Advancing the atomistic understanding of CaM and SK2 interaction by structural modeling and MD simulations

Apo-CaM binding to the CaMBD of SK channels requires the C-lobe, while binding of Ca^{2+} to the N-lobe is involved in SK channel gating (Keen et al., 1999). Several human CaM mutations affect the activation of SK channels (Yu et al., 2016). However, the exact mechanisms among the different CaM mutations remain incompletely understood. Our study shows a significant reduction of cardiac SK currents by CaM_{D96V} and CaM_{D130G}, not only in the hetero-expression system but also in endogenous SK currents in hiPSC-CMs, consistent with DN effects on channel function.

In contrast, phenylalanine mutations in CaM disrupt interaction between apo-CaM and the SK channel without the DN effects. Rosetta molecular modeling is used by taking advantage of the recently published cryo-EM structure of the SK4–apo-CaM complex (Lee and MacKinnon, 2018). We identified the interactions of three key phenylalanine residues (Phe^{90}, Phe^{93}, and Phe^{142}) within the C-lobe of apo-CaM, with hydrophobic amino acids in the CaMBD within the C terminus of the SK2 channel. In addition, previous studies have shown reduced binding affinity to RYR2 by CaM_{F90L}. Circular dichroism experiments in the same study suggest C-lobe destabilization and decreased Ca^{2+}-binding affinity (Nomikos et al., 2014). Our molecular modeling of the CaM_{F90L} mutant shows a significant deviation from CaM_{WT} in the C-lobe structure in the Ca^{2+}-free state (Fig. 6). Taken together with biochemical and functional analyses, the results suggest that the Phe mutations primarily disrupt apo-CaM interactions with the SK2 CaMBD. Indeed, despite significant conformational changes, there were only modest inhibitory effects on apamin-sensitive currents (Fig. 3), consistent with a lack of DN effects; in contrast to CaM_{D96V} and CaM_{D130G} mutants.

Structural modeling and MD simulations provide critical insights into the atomistic mechanisms of CaM mutants in human calmodulinopathy. Our findings suggest that all three Phe mutations in CaM result in similar conformational changes, including an increase in flexibility of the C-terminal end of helix 2, a decrease in flexibility of the C-terminal end of helix 3, and a decrease in the flexibility of the Ca^{2+}-binding site 4 (Fig. 7). The findings support our conclusion that the three Phe → Leu mutations exhibit a similar mechanism in altering the regulation of the hSK2 channel, likely through a reduction in the interaction between apo-CaM and CaMBD in the SK2 channel. These critical insights into the distinct mechanisms whereby these CaM mutations exert their effects on Ca^{2+}-dependent ion channels and cardiac action potential repolarization help to pave the way for understanding the genotype–phenotype correlations of human calmodulinopathy.

Limitations and future directions

RMSD as a metric is circumstantial to derive conclusions on the thermodynamic stability of WT and mutant CaMs. Nonetheless, we have provided additional analyses of RMSF in the current

Downloaded from http://rupress.org/jgp/article-pdf/152/12/e202012667/1800962/jgp_202012667.pdf by guest on 07 February 2026

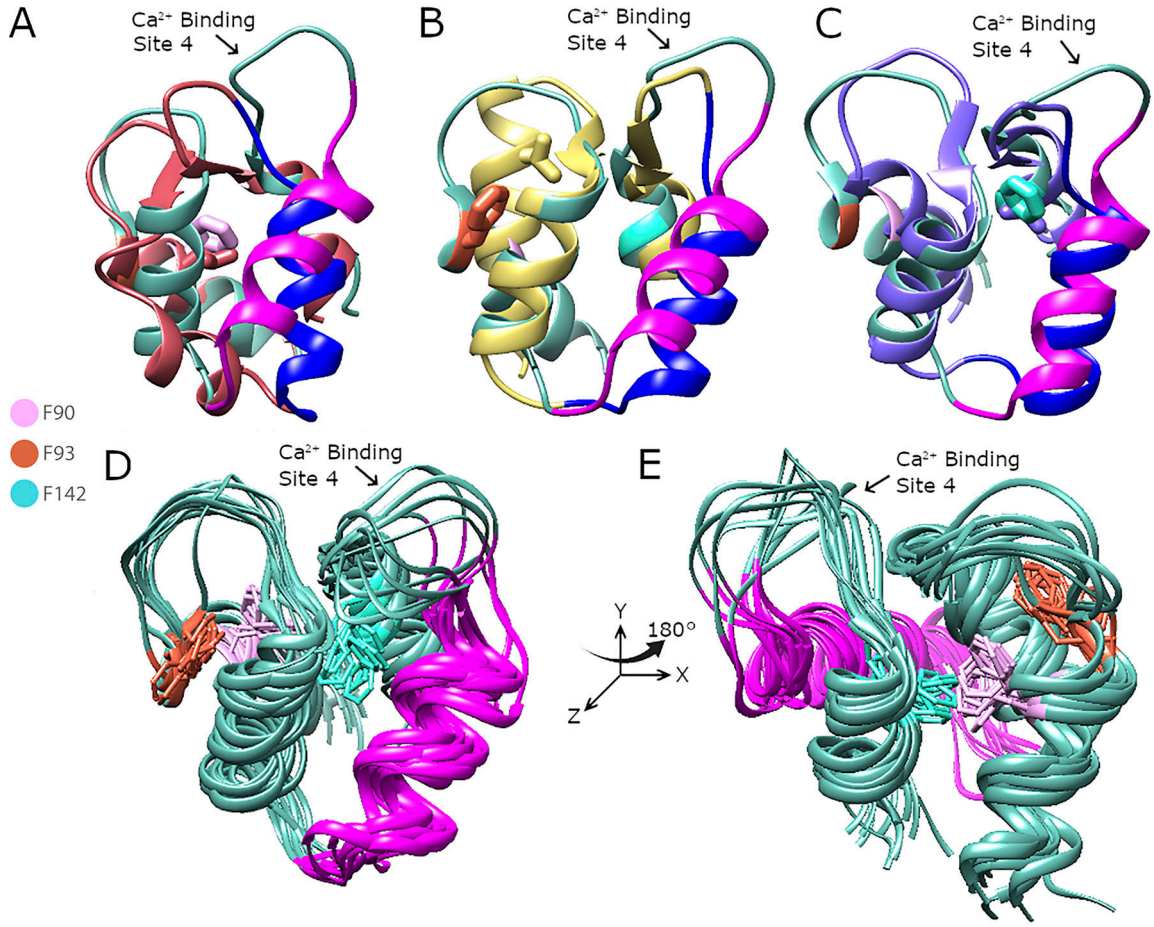

Figure 8. **Graphical comparison from MD simulations of the C-lobe of apo-CaMs showing conformational changes in mutant CaMs with repacking of helices 2 and 3 and highly flexible Ca^{2+}-binding site 4 in apo-CaM_{WT} compared with the mutant CaMs, confirming the RMSF results. (A–C)** Top clustered models of the C-lobe of apo-CaM_{F90L} (red), apo-CaM_{F93L} (yellow), and apo-CaM_{F142L} (purple) are aligned with apo-CaM_{WT} (green) in A, B, and C, respectively. Amino acid side chains of Phe^{90} (pink) and F90L (red) from apo-CaM_{WT} and apo-CaM_{F90L} (A), amino acid side chains of Phe^{93} (red) and F93L (yellow) from apo-CaM_{WT} and apo-CaM_{F93L} (B), and amino acid side chains of Phe^{142} (light blue) and F142L (light purple) from apo-CaM_{WT} and apo-CaM_{F90L} (C) are shown in the stick representation. Helix 3 from apo-CaM_{WT} (magenta) resides at a larger angle in reference to the y axis compared with helices 3 from Phe → Leu mutant CaMs (dark blue) in A, B, and C, consistent with repacking of the structures. Quantification of the differences between apo-CaM_{WT} and mutant CaMs shown in A, B, and C are summarized in Table S2. **(D)** Top 10 clustered models of apo-CaM_{WT} aligned to represent an ensemble of possible states. Amino acid representation and color are conserved from A–C. Helix 3 is in purple. Helix 3 is mostly in a similar angle in reference to the y axis, with a much more extreme model present in the distribution. In addition, Ca^{2+}-binding site 4 has a wide distribution of states, which does not align with those from the mutants (A–C). **(E)** Panel D rotated 180° to the right around the y axis.

study. Future studies are needed to derive free-energy calculations of the mutations compared with CaM_{WT}. The alteration in flexibility and the possible effects of the mutations on Ca^{2+}-binding site 4 and their cooperativity with other Ca^{2+}-binding sites require further studies as an underlying mechanism affecting CaM mutations. Future studies are needed to test the possible roles of hydrogen bonds between the side chain of Asn^{112} with the carboxyl oxygen of the Ala^{89} residue in apo-CaM_{WT}, which is lost in all three Phe → Leu mutations based on MD simulations.

Additionally, studies evaluating the effects of CaM mutants in native cells would be ideal; however, the study of mutant proteins within endogenous cells is not without difficulties. To circumvent these issues, the study of CaM mutants in cardiomyocyte-like cells may yet yield valuable information. Consequently, patient-specific hiPSC-CMs may provide additional insights into the effects of CaM mutants on SK channels and action potential profiles. Finally, future studies using CRISPR/Cas9 gene editing would help to further elucidate the effects of CaM mutations on SK channel function.

Acknowledgments

Jeanne M. Nerbonne served as editor.

This work is funded in part by the American Heart Association Beginning Grant-in-Aid 14BGIA18870087 and National Institutes of Health (NIH) grants R56 HL138392 (to X.-D. Zhang); R01 HL085727, R01 HL085844, and R01 HL137228 (to N. Chiamvimonvat); R01 HL083374 (to A.L. George Jr.); R35 HL144980 (to B.C. Knollmann); and R01 DC015135, R01 DC015252, R01 DC016099, and P01 AG051443 (to E.N. Yamoah); and United States Department of Veterans Affairs Merit Review

Downloaded from http://rupress.org/jgp/article-pdf/152/12/e202012667/1800962/jgp_202012667.pdf by guest on 07 February 2026

Grants I01 BX000576 and I01 CX001490 (to N. Chiamvimonvat). H.A. Ledford received a Predoctoral Fellowship from NIH/National Heart, Lung, and Blood Institute (NHLBI) Institutional Training Grant in Basic and Translational Cardiovascular Science (T32 HL086350 and F31 HL136120). R.L. Woltz received a Postdoctoral Fellowships from NIH/NHLBI (F32 HL151130). L. Ren received a Predoctoral Fellowship from the American Heart Association. P. Sirish received a Postdoctoral Fellowship from California Institute for Regenerative Medicine Training Grant to University of California Davis and NIH/NHLBI Institutional Training Grant in Basic and Translational Cardiovascular Science (T32 HL086350), an American Heart Association Career Development Award, and the Harold S. Geneen Charitable Trust Award. N. Chiamvimonvat is the holder of the Roger Tatarian Endowed Professorship in Cardiovascular Medicine and a part-time staff physician at VA Northern California Health Care System, Mather, CA.

The authors declare no competing financial interests.

Author contributions: H.A. Ledford, W. Wang, and X.-D. Zhang performed the electrophysiological experiments and analyzed and interpreted the data. H.A. Ledford, S. Park, L. Ren, and C.-R. Sihn performed the molecular cloning and biochemical experiments. R.L. Woltz, D. Muir, P.T. Nguyen, and V. Yarov-Yarovoy performed the structural modeling and MD simulations. H.A. Ledford performed immunofluorescence imaging. P. Sirish performed stem cell differentiation. H.A. Ledford, X.-D. Zhang, P.T. Nguyen, E.N. Yamoah, V. Yarov-Yarovoy, and N. Chiamvimonvat wrote the manuscript. A.L. George, Jr. and B.C. Knollman provided critical reagents for the study. H.A. Ledford, E.N. Yamoah, X.-D. Zhang, and N. Chiamvimonvat conceived the project, designed the experiments, interpreted the data, and wrote the manuscript.

Submitted: 6 June 2020
Revised: 25 August 2020
Accepted: 19 October 2020

References

Alford, R.F., A. Leaver-Fay, J.R. Jeliazkov, M.J. O'Meara, F.P. DiMaio, H. Park, M.V. Shapovalov, P.D. Renfrew, V.K. Mulligan, K. Kappel, et al. 2017. The Rosetta All-Atom Energy Function for Macromolecular Modeling and Design. *J. Chem. Theory Comput.* 13:3031–3048. https://doi.org/10.1021/acs.jctc.7b00125

Babu, Y.S., J.S. Sack, T.J. Greenhough, C.E. Bugg, A.R. Means, and W.J. Cook. 1985. Three-dimensional structure of calmodulin. *Nature.* 315:37–40. https://doi.org/10.1038/315037a0

Bender, B.J., A. Cisneros III, A.M. Duran, J.A. Finn, D. Fu, A.D. Lokits, B.K. Mueller, A.K. Sangha, M.F. Sauer, A.M. Sevy, et al. 2016. Protocols for Molecular Modeling with Rosetta3 and RosettaScripts. *Biochemistry.* 55:4748–4763. https://doi.org/10.1021/acs.biochem.6b00444

Boczek, N.J., N. Gomez-Hurtado, D. Ye, M.L. Calvert, D.J. Tester, D. Kryshtal, H.S. Hwang, C.N. Johnson, W.J. Chazin, C.G. Loporcaro, et al. 2016. Spectrum and Prevalence of CALM1-, CALM2-, and CALM3-Encoded Calmodulin Variants in Long QT Syndrome and Functional Characterization of a Novel Long QT Syndrome-Associated Calmodulin Missense Variant, E141G. *Circ. Cardiovasc. Genet.* 9:136–146. https://doi.org/10.1161/CIRCGENETICS.115.001323

Bonneau, R., C.E. Strauss, and D. Baker. 2001. Improving the performance of Rosetta using multiple sequence alignment information and global measures of hydrophobic core formation. *Proteins.* 43:1–11. https://doi.org/10.1002/1097-0134(20010401)43:1<1::AID-PROT1012>3.0.CO;2-A

Brooks, B.R., C.L. Brooks III, A.D. Mackerell Jr., L. Nilsson, R.J. Petrella, B. Roux, Y. Won, G. Archontis, C. Bartels, S. Boresch, et al. 2009. CHARMM: the biomolecular simulation program. *J. Comput. Chem.* 30:1545–1614. https://doi.org/10.1002/jcc.21287

Chan, Y.H., W.C. Tsai, J.S. Ko, D. Yin, P.C. Chang, M. Rubart, J.N. Weiss, T.H. Everett IV, S.F. Lin, and P.S. Chen. 2015. Small-Conductance Calcium-Activated Potassium Current Is Activated During Hypokalemia and Masks Short-Term Cardiac Memory Induced by Ventricular Pacing. *Circulation.* 132:1377–1386. https://doi.org/10.1161/CIRCULATIONAHA.114.015125

Chang, P.C., I. Turker, J.C. Lopshire, S. Masroor, B.L. Nguyen, W. Tao, M. Rubart, P.S. Chen, Z. Chen, and T. Ai. 2013. Heterogeneous upregulation of apamin-sensitive potassium currents in failing human ventricles. *J. Am. Heart Assoc.* 2:e004713. https://doi.org/10.1161/JAHA.112.004713

Chin, D., and A.R. Means. 2000. Calmodulin: a prototypical calcium sensor. *Trends Cell Biol.* 10:322–328. https://doi.org/10.1016/S0962-8924(00)01800-6

Chua, S.K., P.C. Chang, M. Maruyama, I. Turker, T. Shinohara, M.J. Shen, Z. Chen, C. Shen, M. Rubart-von der Lohe, J.C. Lopshire, et al. 2011. Small-conductance calcium-activated potassium channel and recurrent ventricular fibrillation in failing rabbit ventricles. *Circ. Res.* 108:971–979. https://doi.org/10.1161/CIRCRESAHA.110.238386

Crivici, A., and M. Ikura. 1995. Molecular and structural basis of target recognition by calmodulin. *Annu. Rev. Biophys. Biomol. Struct.* 24:85–116. https://doi.org/10.1146/annurev.bb.24.060195.000505

Crotti, L., C.N. Johnson, E. Graf, G.M. De Ferrari, B.F. Cuneo, M. Ovadia, J. Papagiannis, M.D. Feldkamp, S.G. Rathi, J.D. Kunic, et al. 2013. Calmodulin mutations associated with recurrent cardiac arrest in infants. *Circulation.* 127:1009–1017. https://doi.org/10.1161/CIRCULATIONAHA.112.001216

Cukovic, D., G.W. Lu, B. Wible, D.F. Steele, and D. Fedida. 2001. A discrete amino terminal domain of Kv1.5 and Kv1.4 potassium channels interacts with the spectrin repeats of alpha-actinin-2. *FEBS Lett.* 498:87–92. https://doi.org/10.1016/S0014-5793(01)02505-4

Darden, T., D. York, and L. Pedersen. 1993. Particle mesh Ewald: An N.log(N) method for Ewald sums in large systems. *J. Chem. Phys.* 98:10089–10092. https://doi.org/10.1063/1.464397

Diness, J.G., B.H. Bentzen, U.S. Sørensen, and M. Grunnet. 2015. Role of Calcium-activated Potassium Channels in Atrial Fibrillation Pathophysiology and Therapy. *J. Cardiovasc. Pharmacol.* 66:441–448. https://doi.org/10.1097/FJC.0000000000000249

Findeisen, F., and D.L. Minor. 2010. Progress in the structural understanding of voltage-gated calcium channel (CaV) function and modulation. *Channels (Austin).* 4:459–474. https://doi.org/10.4161/chan.4.6.12867

Fukuda, M., T. Yamamoto, S. Nishimura, T. Kato, W. Murakami, A. Hino, M. Ono, H. Tateishi, T. Oda, S. Okuda, et al. 2014. Enhanced binding of calmodulin to RyR2 corrects arrhythmogenic channel disorder in CPVT-associated myocytes. *Biochem. Biophys. Res. Commun.* 448:1–7. https://doi.org/10.1016/j.bbrc.2014.03.152

George, A.L. Jr. 2015. Calmodulinopathy: a genetic trilogy. *Heart Rhythm.* 12:423–424. https://doi.org/10.1016/j.hrthm.2014.11.017

Haïssaguerre, M., D.C. Shah, P. Jaïs, M. Shoda, J. Kautzner, T. Arentz, D. Kalushe, A. Kadish, M. Griffith, F. Gaïta, et al. 2002. Role of Purkinje conducting system in triggering of idiopathic ventricular fibrillation. *Lancet.* 359:677–678. https://doi.org/10.1016/S0140-6736(02)07807-8

Halling, D.B., P. Aracena-Parks, and S.L. Hamilton. 2006. Regulation of voltage-gated Ca^{2+} channels by calmodulin. *Sci. STKE.* 2006:er1.

Heidorn, D.B., and J. Trewhella. 1988. Comparison of the crystal and solution structures of calmodulin and troponin C. *Biochemistry.* 27:909–915. https://doi.org/10.1021/bi00403a011

Huang, J., S. Rauscher, G. Nawrocki, T. Ran, M. Feig, B.L. de Groot, H. Grubmüller, and A.D. MacKerell Jr. 2017. CHARMM36m: an improved force field for folded and intrinsically disordered proteins. *Nat. Methods.* 14:71–73. https://doi.org/10.1038/nmeth.4067

Humphrey, W., A. Dalke, and K. Schulten. 1996. VMD: visual molecular dynamics. *J. Mol. Graph.* 14:33–38: 27–28. https://doi.org/10.1016/0263-7855(96)00018-5

Hwang, H.S., F.R. Nitu, Y. Yang, K. Walweel, L. Pereira, C.N. Johnson, M. Faggioni, W.J. Chazin, D. Laver, A.L. George Jr., et al. 2014. Divergent regulation of ryanodine receptor 2 calcium release channels by arrhythmogenic human calmodulin missense mutants. *Circ. Res.* 114:1114–1124. https://doi.org/10.1161/CIRCRESAHA.114.303391

Ishii, T.M., C. Silvia, B. Hirschberg, C.T. Bond, J.P. Adelman, and J. Maylie. 1997. A human intermediate conductance calcium-activated potassium

Downloaded from http://rupress.org/jgp/article-pdf/152/12/e202012667/1800962/jgp_202012667.pdf by guest on 07 February 2026

channel. *Proc. Natl. Acad. Sci. USA.* 94:11651–11656. https://doi.org/10.1073/pnas.94.21.11651

Jensen, H.H., M. Brohus, M. Nyegaard, and M.T. Overgaard. 2018. Human Calmodulin Mutations. *Front. Mol. Neurosci.* 11:396. https://doi.org/10.3389/fnmol.2018.00396

Jo, S., T. Kim, V.G. Iyer, and W. Im. 2008. CHARMM-GUI: a web-based graphical user interface for CHARMM. *J. Comput. Chem.* 29:1859–1865. https://doi.org/10.1002/jcc.20945

Joiner, W.J., L.Y. Wang, M.D. Tang, and L.K. Kaczmarek. 1997. hSK4, a member of a novel subfamily of calcium-activated potassium channels. *Proc. Natl. Acad. Sci. USA.* 94:11013–11018. https://doi.org/10.1073/pnas.94.20.11013

Keen, J.E., R. Khawaled, D.L. Farrens, T. Neelands, A. Rivard, C.T. Bond, A. Janowsky, B. Fakler, J.P. Adelman, and J. Maylie. 1999. Domains responsible for constitutive and $Ca^{(2+)}$-dependent interactions between calmodulin and small conductance $Ca^{(2+)}$-activated potassium channels. *J. Neurosci.* 19:8830–8838. https://doi.org/10.1523/JNEUROSCI.19-20-08830.1999

Kim, H.J., P. Lv, C.R. Sihn, and E.N. Yamoah. 2011. Cellular and molecular mechanisms of autosomal dominant form of progressive hearing loss, *DFNA2*. *J. Biol. Chem.* 286:1517–1527. https://doi.org/10.1074/jbc.M110.179010

Klevit, R.E., D.C. Dalgarno, B.A. Levine, and R.J. Williams. 1984. 1H-NMR studies of calmodulin. The nature of the Ca2+-dependent conformational change. *Eur. J. Biochem.* 139:109–114. https://doi.org/10.1111/j.1432-1033.1984.tb07983.x

Ko, J.S., S. Guo, J. Hassel, P. Celestino-Soper, T.C. Lynnes, J.E. Tisdale, J.J. Zheng, S.E. Taylor, T. Foroud, M.D. Murray, et al. 2018. Ondansetron blocks wild-type and p.F503L variant small-conductance Ca^{2+}-activated K^+ channels. *Am. J. Physiol. Heart Circ. Physiol.* 315:H375–H388. https://doi.org/10.1152/ajpheart.00479.2017

Köhler, M., B. Hirschberg, C.T. Bond, J.M. Kinzie, N.V. Marrion, J. Maylie, and J.P. Adelman. 1996. Small-conductance, calcium-activated potassium channels from mammalian brain. *Science.* 273:1709–1714. https://doi.org/10.1126/science.273.5282.1709

Lee, C.H., and R. MacKinnon. 2018. Activation mechanism of a human SK-calmodulin channel complex elucidated by cryo-EM structures. *Science.* 360:508–513. https://doi.org/10.1126/science.aas9466

Lee, J., X. Cheng, J.M. Swails, M.S. Yeom, P.K. Eastman, J.A. Lemkul, S. Wei, J. Buckner, J.C. Jeong, Y. Qi, et al. 2016. CHARMM-GUI Input Generator for NAMD, GROMACS, AMBER, OpenMM, and CHARMM/OpenMM Simulations Using the CHARMM36 Additive Force Field. *J. Chem. Theory Comput.* 12:405–413. https://doi.org/10.1021/acs.jctc.5b00935

Liang, H., C.D. DeMaria, M.G. Erickson, M.X. Mori, B.A. Alseikhan, and D.T. Yue. 2003. Unified mechanisms of Ca2+ regulation across the Ca^{2+} channel family. *Neuron.* 39:951–960. https://doi.org/10.1016/S0896-6273(03)00560-9

Limpitikul, W.B., I.E. Dick, R. Joshi-Mukherjee, M.T. Overgaard, A.L. George Jr., and D.T. Yue. 2014. Calmodulin mutations associated with long QT syndrome prevent inactivation of cardiac L-type $Ca^{(2+)}$ currents and promote proarrhythmic behavior in ventricular myocytes. *J. Mol. Cell. Cardiol.* 74:115–124. https://doi.org/10.1016/j.yjmcc.2014.04.022

Lu, L., Q. Zhang, V. Timofeyev, Z. Zhang, J.N. Young, H.S. Shin, A.A. Knowlton, and N. Chiamvimonvat. 2007. Molecular coupling of a Ca^{2+}-activated K^+ channel to L-type Ca^{2+} channels via alpha-actinin2. *Circ. Res.* 100:112–120. https://doi.org/10.1161/01.RES.0000253095.44186.72

Lu, L., V. Timofeyev, N. Li, S. Rafizadeh, A. Singapuri, T.R. Harris, and N. Chiamvimonvat. 2009. Alpha-actinin2 cytoskeletal protein is required for the functional membrane localization of a Ca^{2+}-activated K^+ channel (SK2 channel). *Proc. Natl. Acad. Sci. USA.* 106:18402–18407. https://doi.org/10.1073/pnas.0908207106

Meissner, G. 1986. Ryanodine activation and inhibition of the Ca^{2+} release channel of sarcoplasmic reticulum. *J. Biol. Chem.* 261:6300–6306.

Mori, M.X., M.G. Erickson, and D.T. Yue. 2004. Functional stoichiometry and local enrichment of calmodulin interacting with Ca^{2+} channels. *Science.* 304:432–435. https://doi.org/10.1126/science.1093490

Nomikos, M., A. Thanassoulas, K. Beck, V. Vassilakopoulou, H. Hu, B.L. Calver, M. Theodoridou, J. Kashir, L. Blayney, E. Livaniou, et al. 2014. Altered RyR2 regulation by the calmodulin F90L mutation associated with idiopathic ventricular fibrillation and early sudden cardiac death. *FEBS Lett.* 588:2898–2902. https://doi.org/10.1016/j.febslet.2014.07.007

Nyegaard, M., M.T. Overgaard, M.T. Søndergaard, M. Vranas, E.R. Behr, L.L. Hildebrandt, J. Lund, P.L. Hedley, A.J. Camm, G. Wettrell, et al. 2012. Mutations in calmodulin cause ventricular tachycardia and sudden cardiac death. *Am. J. Hum. Genet.* 91:703–712. https://doi.org/10.1016/j.ajhg.2012.08.015

Ozgen, N., W. Dun, E.A. Sosunov, E.P. Anyukhovsky, M. Hirose, H.S. Duffy, P.A. Boyden, and M.R. Rosen. 2007. Early electrical remodeling in rabbit pulmonary vein results from trafficking of intracellular SK2 channels to membrane sites. *Cardiovasc. Res.* 75:758–769. https://doi.org/10.1016/j.cardiores.2007.05.008

Peterson, B.Z., C.D. DeMaria, J.P. Adelman, and D.T. Yue. 1999. Calmodulin is the Ca^{2+} sensor for Ca^{2+}-dependent inactivation of L-type calcium channels. *Neuron.* 22:549–558. https://doi.org/10.1016/S0896-6273(00)80709-6

Pettersen, E.F., T.D. Goddard, C.C. Huang, G.S. Couch, D.M. Greenblatt, E.C. Meng, and T.E. Ferrin. 2004. UCSF Chimera--a visualization system for exploratory research and analysis. *J. Comput. Chem.* 25:1605–1612. https://doi.org/10.1002/jcc.20084

Phillips, J.C., R. Braun, W. Wang, J. Gumbart, E. Tajkhorshid, E. Villa, C. Chipot, R.D. Skeel, L. Kalé, and K. Schulten. 2005. Scalable molecular dynamics with NAMD. *J. Comput. Chem.* 26:1781–1802. https://doi.org/10.1002/jcc.20289

Qi, X.Y., J.G. Diness, B.J. Brundel, X.B. Zhou, P. Naud, C.T. Wu, H. Huang, M. Harada, M. Aflaki, D. Dobrev, et al. 2014. Role of small-conductance calcium-activated potassium channels in atrial electrophysiology and fibrillation in the dog. *Circulation.* 129:430–440. https://doi.org/10.1161/CIRCULATIONAHA.113.003019

Rafizadeh, S., Z. Zhang, R.L. Woltz, H.J. Kim, R.E. Myers, L. Lu, D. Tuteja, A. Singapuri, A.A. Bigdeli, S.B. Harchache, et al. 2014. Functional interaction with filamin A and intracellular Ca^{2+} enhance the surface membrane expression of a small-conductance Ca^{2+}-activated K^+ (SK2) channel. *Proc. Natl. Acad. Sci. USA.* 111:9989–9994. https://doi.org/10.1073/pnas.1323541111

Reed, G.J., N.J. Boczek, S.P. Etheridge, and M.J. Ackerman. 2015. CALM3 mutation associated with long QT syndrome. *Heart Rhythm.* 12:419–422. https://doi.org/10.1016/j.hrthm.2014.10.035

Reher, T.A., Z. Wang, C.H. Hsueh, P.C. Chang, Z. Pan, M. Kumar, J. Patel, J. Tan, C. Shen, Z. Chen, et al. 2017. Small-Conductance Calcium-Activated Potassium Current in Normal Rabbit Cardiac Purkinje Cells. *J. Am. Heart Assoc.* 6:e005471. https://doi.org/10.1161/JAHA.117.005471

Rohl, C.A., C.E. Strauss, K.M. Misura, and D. Baker. 2004. Protein structure prediction using Rosetta. *Methods Enzymol.* 383:66–93. https://doi.org/10.1016/S0076-6879(04)83004-0

Roselli, C., M.D. Chaffin, L.C. Weng, S. Aeschbacher, G. Ahlberg, C.M. Albert, P. Almgren, A. Alonso, C.D. Anderson, K.G. Aragam, et al. 2018. Multi-ethnic genome-wide association study for atrial fibrillation. *Nat. Genet.* 50:1225–1233. https://doi.org/10.1038/s41588-018-0133-9

Sachyani, D., M. Dvir, R. Strulovich, G. Tria, W. Tobelaim, A. Peretz, O. Pongs, D. Svergun, B. Attali, and J.A. Hirsch. 2014. Structural basis of a $K_v7.1$ potassium channel gating module: studies of the intracellular c-terminal domain in complex with calmodulin. *Structure.* 22:1582–1594. https://doi.org/10.1016/j.str.2014.07.016

Saimi, Y., and C. Kung. 2002. Calmodulin as an ion channel subunit. *Annu. Rev. Physiol.* 64:289–311. https://doi.org/10.1146/annurev.physiol.64.100301.111649

Saljic, A., K.M. Muthukumarasamy, J.M. la Cour, K. Boddum, M. Grunnet, M.W. Berchtold, and T. Jespersen. 2019. Impact of arrhythmogenic calmodulin variants on small conductance Ca^{2+}-activated K^+ (SK3) channels. *Physiol. Rep.* 7:e14210. https://doi.org/10.14814/phy2.14210

Schumacher, M.A., A.F. Rivard, H.P. Bächinger, and J.P. Adelman. 2001. Structure of the gating domain of a Ca2+-activated K+ channel complexed with Ca2+/calmodulin. *Nature.* 410:1120–1124. https://doi.org/10.1038/35074145

Shamgar, L., L. Ma, N. Schmitt, Y. Haitin, A. Peretz, R. Wiener, J. Hirsch, O. Pongs, and B. Attali. 2006. Calmodulin is essential for cardiac I_{KS} channel gating and assembly: impaired function in long-QT mutations. *Circ. Res.* 98:1055–1063. https://doi.org/10.1161/01.RES.0000218979.40770.69

Sirish, P., N. Li, V. Timofeyev, X.D. Zhang, L. Wang, J. Yang, K.S. Lee, A. Bettaieb, S.M. Ma, J.H. Lee, et al. 2016. Molecular Mechanisms and New Treatment Paradigm for Atrial Fibrillation. *Circ. Arrhythm. Electrophysiol.* 9:e003721. https://doi.org/10.1161/CIRCEP.115.003721

Sun, J., and R. MacKinnon. 2017. Cryo-EM Structure of a KCNQ1/CaM Complex Reveals Insights into Congenital Long QT Syndrome. *Cell.* 169:1042–1050.e9. https://doi.org/10.1016/j.cell.2017.05.019

Thulin, E., A. Andersson, T. Drakenberg, S. Forsén, and H.J. Vogel. 1984. Metal ion and drug binding to proteolytic fragments of calmodulin: proteolytic, cadmium-113, and proton nuclear magnetic resonance

Downloaded from http://rupress.org/jgp/article-pdf/152/12/e202012667/1800962/jgp_202012667.pdf by guest on 07 February 2026

studies. *Biochemistry*. 23:1862–1870. https://doi.org/10.1021/bi00303a043

Torrente, A.G., R. Zhang, H. Wang, A. Zaini, B. Kim, X. Yue, K.D. Philipson, and J.I. Goldhaber. 2017. Contribution of small conductance K^+ channels to sinoatrial node pacemaker activity: insights from atrial-specific Na^+/Ca^{2+} exchange knockout mice. *J. Physiol.* 595:3847–3865. https://doi.org/10.1113/JP274249

Tuteja, D., D. Xu, V. Timofeyev, L. Lu, D. Sharma, Z. Zhang, Y. Xu, L. Nie, A.E. Vázquez, J.N. Young, et al. 2005. Differential expression of small-conductance Ca^{2+}-activated K^+ channels SK1, SK2, and SK3 in mouse atrial and ventricular myocytes. *Am J Physiol Heart Circ Physiol.* 289: H2714-23. https://doi.org/10.1152/ajpheart.00534.2005

Vanommeslaeghe, K., E. Hatcher, C. Acharya, S. Kundu, S. Zhong, J. Shim, E. Darian, O. Guvench, P. Lopes, I. Vorobyov, and A.D. Mackerell Jr. 2010. CHARMM general force field: A force field for drug-like molecules compatible with the CHARMM all-atom additive biological force fields. *J. Comput. Chem.* 31:671–690.

Vassilakopoulou, V., B.L. Calver, A. Thanassoulas, K. Beck, H. Hu, L. Buntwal, A. Smith, M. Theodoridou, J. Kashir, L. Blayney, et al. 2015. Distinctive malfunctions of calmodulin mutations associated with heart RyR2-mediated arrhythmic disease. *Biochim. Biophys. Acta.* 1850:2168–2176. https://doi.org/10.1016/j.bbagen.2015.07.001

Vergara, C., R. Latorre, N.V. Marrion, and J.P. Adelman. 1998. Calcium-activated potassium channels. *Curr. Opin. Neurobiol.* 8:321–329. https://doi.org/10.1016/S0959-4388(98)80056-1

Wang, C., P. Bradley, and D. Baker. 2007. Protein-protein docking with backbone flexibility. *J. Mol. Biol.* 373:503–519. https://doi.org/10.1016/j.jmb.2007.07.050

Wang, K., C. Holt, J. Lu, M. Brohus, K.T. Larsen, M.T. Overgaard, R. Wimmer, and F. Van Petegem. 2018. Arrhythmia mutations in calmodulin cause conformational changes that affect interactions with the cardiac voltage-gated calcium channel. *Proc. Natl. Acad. Sci. USA.* 115: E10556–E10565. https://doi.org/10.1073/pnas.1808733115

Watterson, D.M., F. Sharief, and T.C. Vanaman. 1980. The complete amino acid sequence of the Ca^{2+}-dependent modulator protein (calmodulin) of bovine brain. *J. Biol. Chem.* 255:962–975.

Wilde, A.A.M., H. Garan, and P.A. Boyden. 2019. Role of the Purkinje system in heritable arrhythmias. *Heart Rhythm.* 16:1121–1126. https://doi.org/10.1016/j.hrthm.2019.01.034

Xia, X.-M., B. Fakler, A. Rivard, G. Wayman, T. Johnson-Pais, J.E. Keen, T. Ishii, B. Hirschberg, C.T. Bond, S. Lutsenko, et al. 1998. Mechanism of calcium gating in small-conductance calcium-activated potassium channels. *Nature.* 395:503–507. https://doi.org/10.1038/26758

Xu, Y., D. Tuteja, Z. Zhang, D. Xu, Y. Zhang, J. Rodriguez, L. Nie, H.R. Tuxson, J.N. Young, K.A. Glatter, et al. 2003. Molecular identification and functional roles of a $Ca^{(2+)}$-activated K^+ channel in human and mouse hearts. *J. Biol. Chem.* 278:49085–49094. https://doi.org/10.1074/jbc.M307508200

Yamoah, M.A., M. Moshref, J. Sharma, W.C. Chen, H.A. Ledford, J.H. Lee, K.S. Chavez, W. Wang, J.E. López, D.K. Lieu, et al. 2018. Highly efficient transfection of human induced pluripotent stem cells using magnetic nanoparticles. *Int. J. Nanomedicine.* 13:6073–6078. https://doi.org/10.2147/IJN.S172254

Yarov-Yarovoy, V., J. Schonbrun, and D. Baker. 2006. Multipass membrane protein structure prediction using Rosetta. *Proteins.* 62:1010–1025. https://doi.org/10.1002/prot.20817

Yarov-Yarovoy, V., P.G. DeCaen, R.E. Westenbroek, C.Y. Pan, T. Scheuer, D. Baker, and W.A. Catterall. 2012. Structural basis for gating charge movement in the voltage sensor of a sodium channel. *Proc. Natl. Acad. Sci. USA.* 109:E93–E102. https://doi.org/10.1073/pnas.1118434109

Yu, C.C., J.S. Ko, T. Ai, W.C. Tsai, Z. Chen, M. Rubart, M. Vatta, T.H. Everett IV, A.L. George Jr., and P.S. Chen. 2016. Arrhythmogenic calmodulin mutations impede activation of small-conductance calcium-activated potassium current. *Heart Rhythm.* 13:1716–1723. https://doi.org/10.1016/j.hrthm.2016.05.009

Zhang, Q., V. Timofeyev, L. Lu, N. Li, A. Singapuri, M.K. Long, C.T. Bond, J.P. Adelman, and N. Chiamvimonvat. 2008. Functional roles of a Ca^{2+}-activated K^+ channel in atrioventricular nodes. *Circ. Res.* 102:465–471. https://doi.org/10.1161/CIRCRESAHA.107.161778

Zhang, X.D., D.K. Lieu, and N. Chiamvimonvat. 2015. Small-conductance Ca^{2+}-activated K^+ channels and cardiac arrhythmias. *Heart Rhythm.* 12:1845–1851. https://doi.org/10.1016/j.hrthm.2015.04.046

Zhang, Z., H.A. Ledford, S. Park, W. Wang, S. Rafizadeh, H.J. Kim, W. Xu, L. Lu, V.C. Lau, A.A. Knowlton, et al. 2017. Distinct subcellular mechanisms for the enhancement of the surface membrane expression of SK2 channel by its interacting proteins, α-actinin2 and filamin A. *J. Physiol.* 595:2271–2284. https://doi.org/10.1113/JP272942

Zhang, X.D., Z.A. Coulibaly, W.C. Chen, H.A. Ledford, J.H. Lee, P. Sirish, G. Dai, Z. Jian, F. Chuang, I. Brust-Mascher, et al. 2018. Coupling of SK channels, L-type Ca^{2+} channels, and ryanodine receptors in cardiomyocytes. *Sci. Rep.* 8:4670. https://doi.org/10.1038/s41598-018-22843-3

Zühlke, R.D., G.S. Pitt, K. Deisseroth, R.W. Tsien, and H. Reuter. 1999. Calmodulin supports both inactivation and facilitation of L-type calcium channels. *Nature.* 399:159–162. https://doi.org/10.1038/20200

Zühlke, R.D., G.S. Pitt, R.W. Tsien, and H. Reuter. 2000. Ca^{2+}-sensitive inactivation and facilitation of L-type Ca^{2+} channels both depend on specific amino acid residues in a consensus calmodulin-binding motif in the(α)1C subunit. *J. Biol. Chem.* 275:21121–21129. https://doi.org/10.1074/jbc.M002986200

Downloaded from http://rupress.org/jgp/article-pdf/152/12/e202012667/1800962/jgp_202012667.pdf by guest on 07 February 2026

Supplemental material

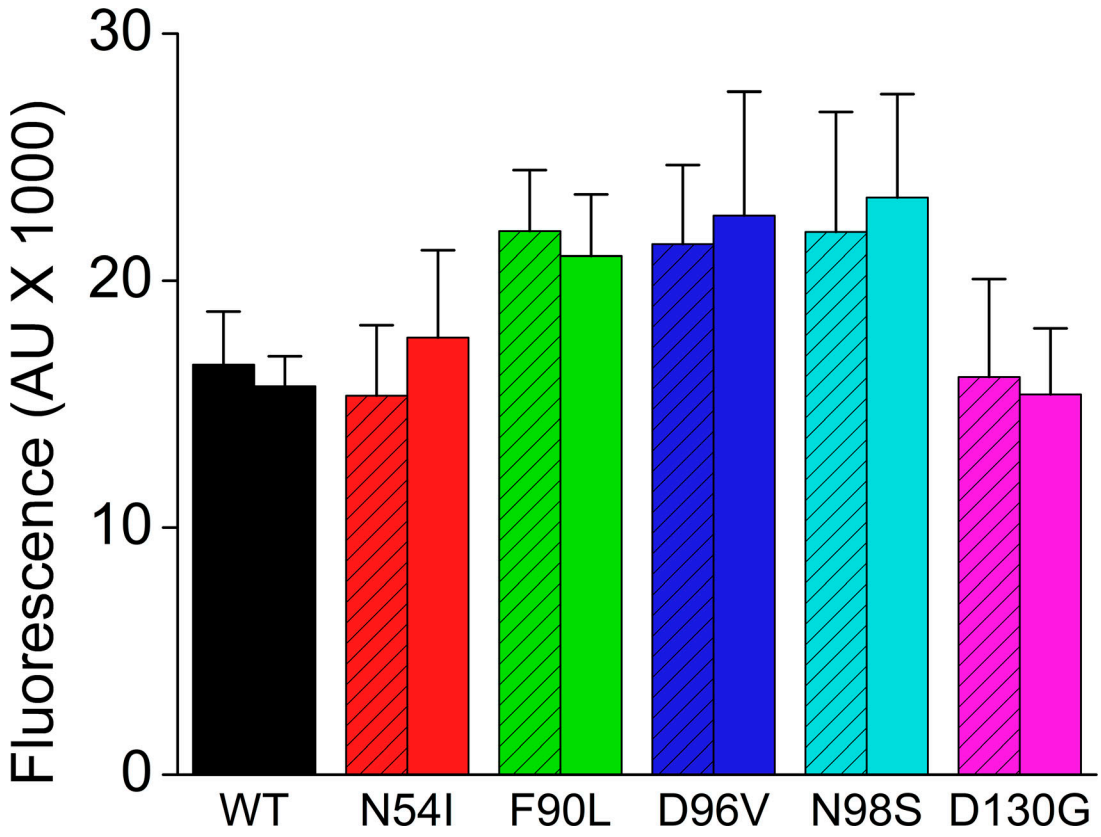

Figure S1. **Trafficking of hSK2 channels after coexpression with CaM_{WT} or mutant CaMs.** HEK 293 cells expressing SK2 fusion protein with HA tag coexpressed with CaM_{WT} or mutant CaMs (N54I, F90L, D96V, N98S, and D130G) using NP and permeabilized conditions. Summary data showing fluorescence intensity under NP (left bars) and permeabilized (right bars) conditions (555 and 633 fluorescent intensities in arbitrary units [AU] × 1,000; *n* = 15–20 cells; P = NS comparing NP with permeabilized for each group). Data shown represents mean ± SEM.

Downloaded from http://rupress.org/jgp/article-pdf/152/12/e202012667/1800962/jgp_202012667.pdf by guest on 07 February 2026

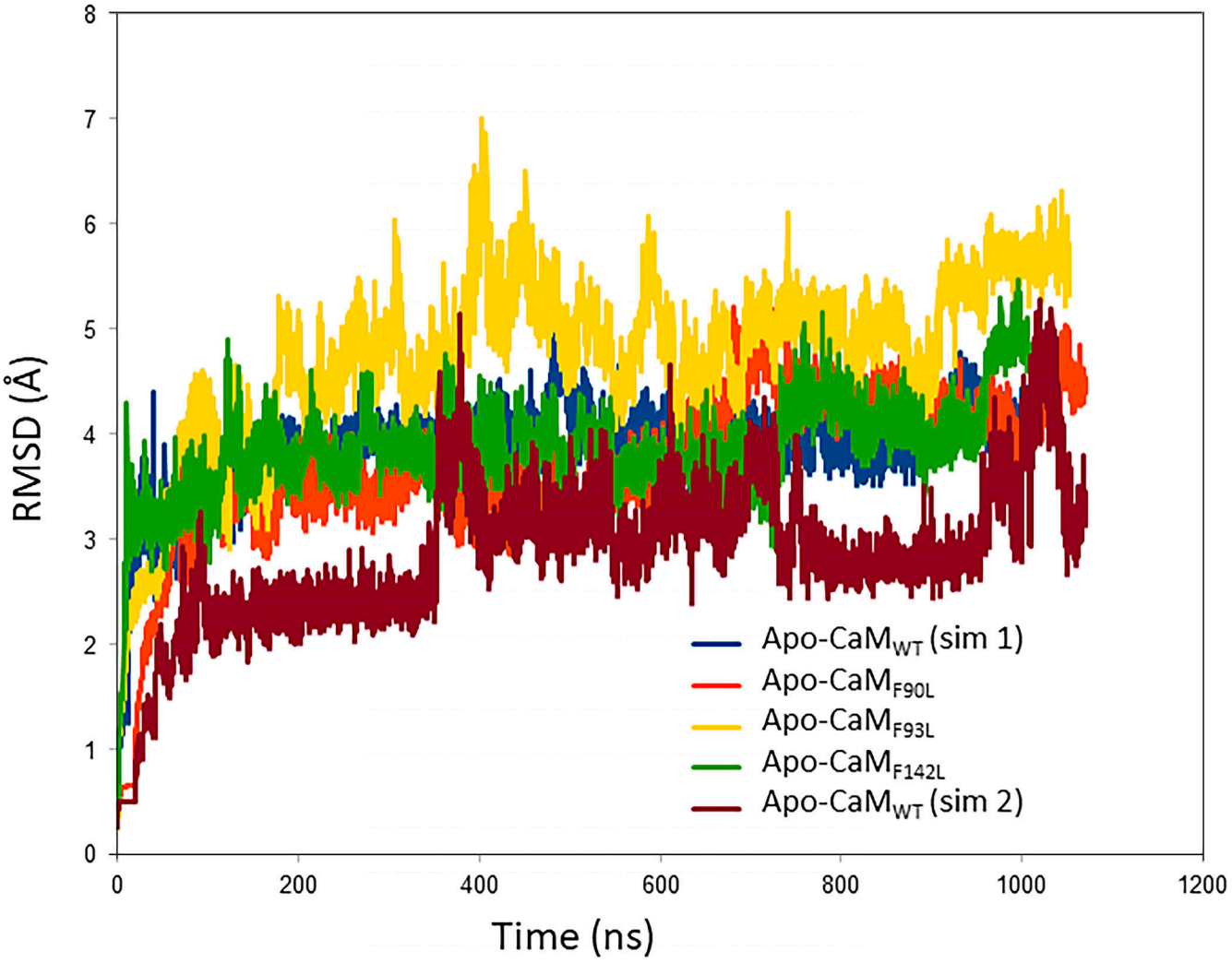

Figure S2. **Graphs of RMSD showing stability throughout the production run.** RMSD graphs include the equilibration and prosecution stages. The RMSD from the C-lobe of apo-CaM$_{WT}$ (simulations [sims] 1 and 2), apo-CaM$_{F90L}$, apo-CaM$_{F93L}$, and apo-CaM$_{F142L}$ are shown in blue, dark brown, red, yellow, and green, respectively. Runs are slightly different in length due to differences in equilibration time. The total simulation time is the same in all runs (1 µs).

Downloaded from http://rupress.org/jgp/article-pdf/152/12/e202012667/1800962/jgp_202012667.pdf by guest on 07 February 2026

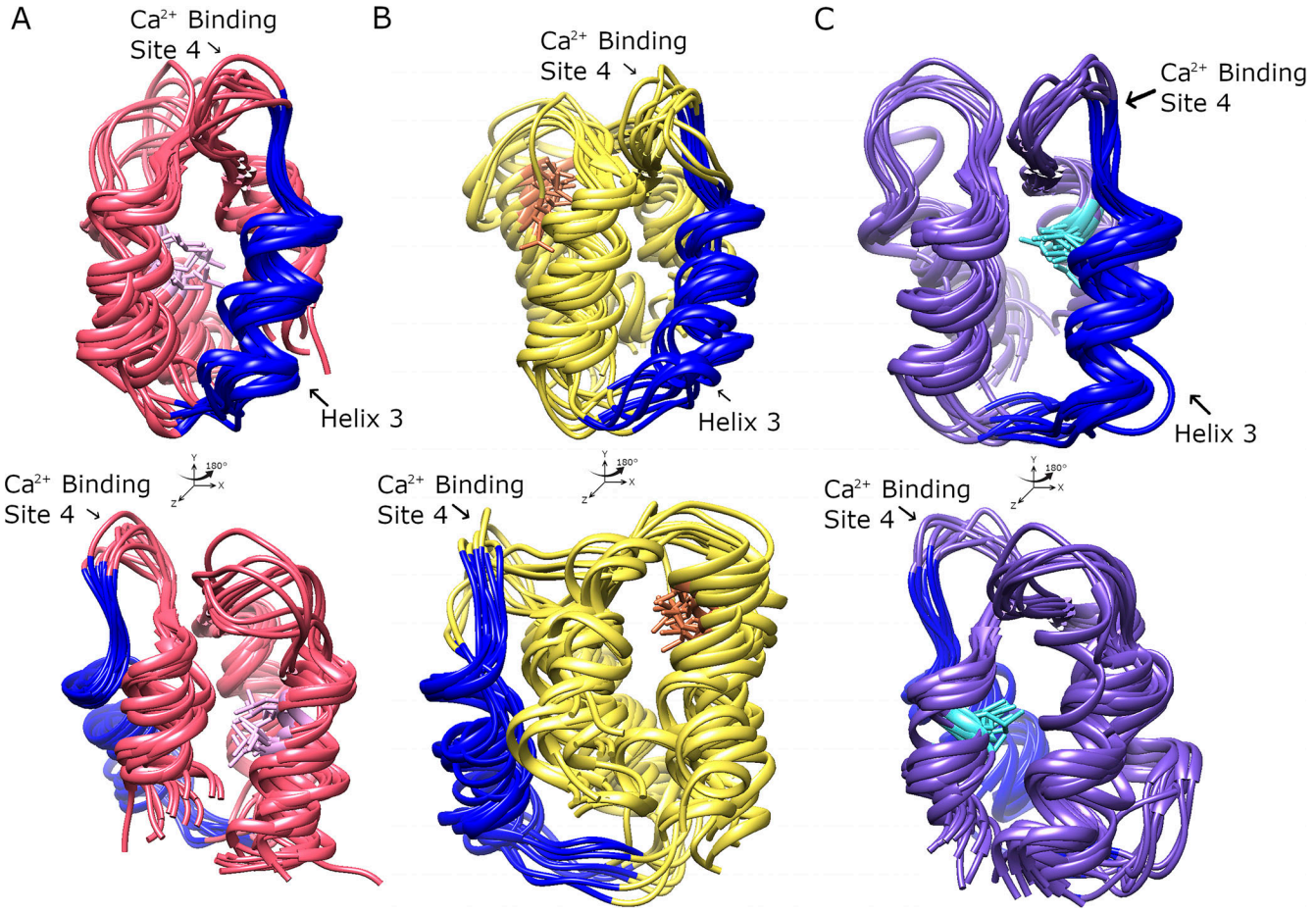

Figure S3. **Top 10 clustered models of the C-lobe of apo-CaM$_{F90L}$, apo-CaM$_{F93L}$, and apo-CaM$_{F142L}$ aligned to represent an ensemble of possible states showing compact distribution of helix 3 and Ca^{2+}-binding site 4 regions.** Ensembles of the aligned top 10 clusters of the C-lobe of apo-CaM$_{F90L}$ (red; A), apo-CaM$_{F93L}$ (yellow; B), and apo-CaM$_{F142L}$ (purple; C). Helix 3 is shown in blue, and the Ca^{2+}-binding site 4 is the loop immediately following helix 3 and is labeled. Lower panels are structures from the upper panels rotated 180° to the right around the y axis.

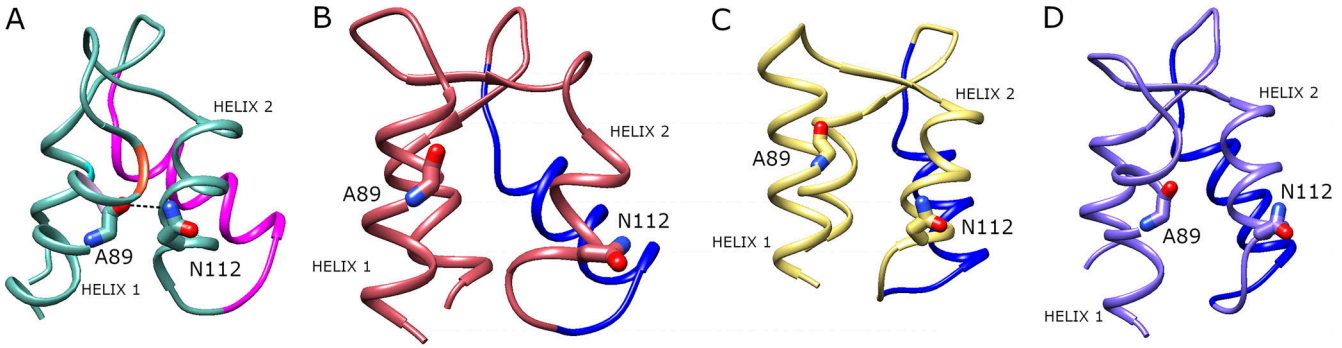

Figure S4. **Graphical comparison from MD simulations of the C-lobe of apo-CaMs showing the hydrogen bond in the apo-CaM$_{WT}$. (A–D)** Top clustered models of the C-lobe of apo-CaM$_{WT}$ (green; A), apo-CaM$_{F90L}$ (red; B), apo-CaM$_{F93L}$ (yellow; C), and apo-CaM$_{F142L}$ (purple; D) are shown. Helix 3 from apo-CaM$_{WT}$ is shown in magenta (A), while helices 3 from Phe → Leu mutant CaMs are shown in dark blue in B–D. The side chain of Asn112 on helix 2 in apo-CaM$_{WT}$ maintains a stable hydrogen bond with the carboxyl oxygen of Ala89 residue on helix 1 during simulations of the apo-CaM$_{WT}$, which is not observed in the simulations of the CaM mutants.

Downloaded from http://rupress.org/jgp/article-pdf/152/12/e202012667/1800962/jgp_202012667.pdf by guest on 07 February 2026

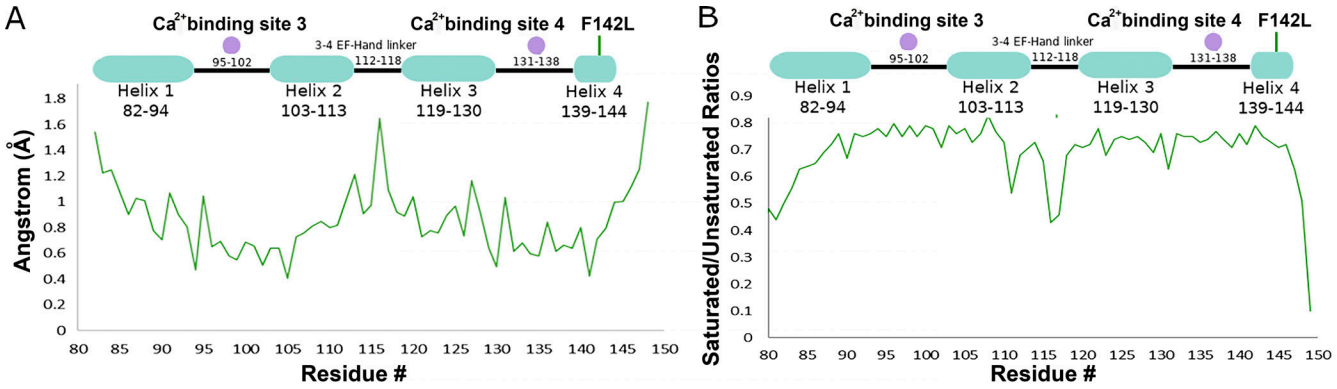

Figure S5. **Comparison of the RMSF of Ca^{2+}-CaM_{F142L} from MD simulations and N-H heteronuclear NOE saturated/unsaturated ratio.** Related to BMRB accession no. 34262; Wang et al., 2018. **(A and B)** There is similar flexibility, including identification of the most flexible amino acid being Lys116 residue. Note: flexibility shown on graphs is inversed, with higher values in RMSF and lower values in heteronuclear NOE denoting higher flexibility.

Video 1. **Morph video from the top Rosetta model of the C-lobe of apo-CaM_{WT} to the top Rosetta model of apo-CaM_{F90L}.** The video illustrates the conformational changes that are required to accommodate a void volume that is created by the phenylalanine-to-leucine mutation, allowing helices 2 and 3 to repack their side chains and readjust their backbone positions. The coloring is the same as in Fig. 6 and Fig. 8 (residues Phe90, Phe93, and Phe142 are shown in pink, red, and light blue, respectively). Helices 2 and 3 are in the foreground, while helices 1 and 4 are in the background. Helix 3 is shown in magenta.

Video 2. **Morph video from the top Rosetta model of the C-lobe of apo-CaM_{WT} to the top Rosetta model of apo-CaM_{F93L}.** The video illustrates the conformational changes that are required to accommodate a void volume that is created by the phenylalanine-to-leucine mutation, allowing helices 2 and 3 to repack their side chains and readjust their backbone positions. The coloring is the same as in Fig. 6 and Fig. 8 (residues Phe90, Phe93, and Phe142 are shown in pink, red, and light blue, respectively). Helices 2 and 3 are in the foreground, while helices 1 and 4 are in the background. Helix 3 is shown in magenta.

Video 3. **Morph video from the top Rosetta model of the C-lobe of apo-CaM_{WT} to the top Rosetta model of apo-CaM_{F142L}.** The video illustrates the conformational changes that are required to accommodate a void volume that is created by the phenylalanine-to-leucine mutation, allowing helices 2 and 3 to repack their side chains and readjust their backbone positions. The coloring is the same as in Fig. 6 and Fig. 8 (residues Phe90, Phe93, and Phe142 are shown in pink, red, and light blue, respectively). Helices 2 and 3 are in the foreground, while helices 1 and 4 are in the background. Helix 3 is shown in magenta.

Video 4. **Morph video from the top MD model of the C-lobe of apo-CaM_{WT} to the top MD model of apo-CaM_{F90L}.** The video illustrates the conformational changes that are required to accommodate a void volume that is created by the phenylalanine-to-leucine mutation, allowing helices 2 and 3 to repack their side chains and readjust their backbone positions. The coloring is the same as in Fig. 6 and Fig. 8 (residues Phe90, Phe93, and Phe142 are shown in pink, red, and light blue, respectively). Helices 2 and 3 are in the foreground, while helices 1 and 4 are in the background. Helix 3 is shown in magenta.

Video 5. **Morph video from the top MD model of the C-lobe of apo-CaM_{WT} to the top MD model of apo-CaM_{F93L}.** The video illustrates the conformational changes that are required to accommodate a void volume that is created by the phenylalanine-to-leucine mutation, allowing helices 2 and 3 to repack their side chains and readjust their backbone positions. The coloring is the same as in Fig. 6 and Fig. 8 (residues Phe90, Phe93, and Phe142 are shown in pink, red, and light blue, respectively). Helices 2 and 3 are in the foreground, while helices 1 and 4 are in the background. Helix 3 is shown in magenta.

Video 6. **Morph video from the top MD model of the C-lobe of apo-CaM_{WT} to the top MD model of apo-CaM_{F142L}.** The video illustrates the conformational changes that are required to accommodate a void volume that is created by the phenylalanine-to-leucine mutation, allowing helices 2 and 3 to repack their side chains and readjust their backbone positions. The coloring is the same as in Fig. 6 and Fig. 8 (residues Phe90, Phe93, and Phe142 are shown in pink, red, and light blue, respectively). Helices 2 and 3 are in the foreground, while helices 1 and 4 are in the background. Helix 3 is shown in magenta.

Downloaded from http://rupress.org/jgp/article-pdf/152/12/e202012667/1800962/jgp_202012667.pdf by guest on 07 February 2026

Provided online are two tables. Table S1 shows quantification of the RMSD calculated from the production portion of MD presented in Fig. S2. Table S2 shows quantification of the differences in the RMSD among WT and mutant CaMs, derived from the C-terminal domain (residues 81–145) and Ca^{2+} binding site 4 (residues 131–138) presented in Fig. 8.

Downloaded from http://rupress.org/jgp/article-pdf/152/12/e202012667/1800962/jgp_202012667.pdf by guest on 07 February 2026